

# Direct pore-scale reactive transport modelling of dynamic wettability changes induced by surface complexation

Julien Maes<sup>a,\*</sup>, Sebastian Geiger<sup>a,b</sup>

<sup>a</sup> Institute of Petroleum Engineering, Heriot-Watt University, Edinburgh, UK

<sup>b</sup> International Center for Carbonate Reservoir (ICCR), UK

## ARTICLE INFO

### Keywords:

Pore-scale modelling  
Wettability change  
Volume-of-fluid  
Reactive transport

## ABSTRACT

Laboratory experiments have shown that oil production from sandstone and carbonate reservoirs by waterflooding could be significantly increased by manipulating the composition of the injected water (e.g. by lowering the ionic strength). Recent studies suggest that a change of wettability induced by a change in surface charge is likely to be one of the driving mechanism of the so-called low-salinity effect. In this case, the potential increase of oil recovery during waterflooding at low ionic strength would be strongly impacted by the inter-relations between flow, transport and chemical reaction at the pore-scale. Hence, a new numerical model that includes two-phase flow, solute reactive transport and wettability alteration is implemented based on the Direct Numerical Simulation of the Navier–Stokes equations and surface complexation modelling. Our model is first used to match experimental results of oil droplet detachment from clay patches. We then study the effect of wettability change on the pore-scale displacement for simple 2D calcite micro-models and evaluate the impact of several parameters such as water composition and injected velocity. Finally, we repeat the simulation experiments on a larger and more complex pore geometry representing a carbonate rock. Our simulations highlight two different effects of low-salinity on oil production from carbonate rocks: a smaller number of oil clusters left in the pores after invasion, and a greater number of pores invaded.

## 1. Introduction

Reactive transport in porous media is an essential field of study in a broad range of applications including oil and gas production, carbon dioxide (CO<sub>2</sub>) sequestration, nuclear waste storage and transport of pollutant in the subsurface (Steeff et al., 2005). Porosity and wettability changes induced by chemical reactions is relevant to a range of production-related applications for oil and gas reservoirs, including diagenesis, well stimulation and Enhanced Oil Recovery (EOR). These processes are particularly important in the case of carbonate reservoirs for which recovery factors generally do not exceed 30%. EOR processes such as CO<sub>2</sub> flooding (Han and Gu, 2014) and Low Salinity Flooding (LSF) (Mahani et al., 2015b) have the potential to significantly increase the recovery factors by changing flow properties such as viscosity and wettability, and increase the overall sweep efficiency in the reservoir.

The coupling between chemical reactions and transport is traditionally described at the macro-scale by an Advection-Dispersion-Reaction Equation (ADRE). However, at the macro-scale, the ADRE has been shown to give inaccurate predictions of experimental results (Gramling et al., 2002). This discrepancy has been linked with

incomplete mixing of the injected and resident fluids (Alhashmi et al., 2015; Karadimitriou et al., 2017). Therefore, modelling the reactive transport at the pore-scale, where the mixing can be resolved on a pore-by-pore level, is a crucial tool to better constrain macroscopic reactions (Zaretskiy et al., 2010).

Although pore-scale non-reactive (Bijeljic et al., 2013; Hosa et al., 2016; Kallel et al., 2016) and reactive transport (Alhashmi et al., 2015; Soulaïne and Tchepeli, 2016; Zaretskiy et al., 2012) have been studied extensively in recent years, only a few studies have included wettability alteration. Kallel et al. (2017) developed a model for wettability alteration during primary drainage based on polar compound adsorption. Watson et al. (2017) included wettability alteration with increasing tracer concentration following a Heaviside function for the contact angle. None of these studies included the geochemical reactions that are taking place at the water/mineral interface and can influence wettability. One of the reasons for this is that wettability change induced by manipulating the injected water composition (e.g. lowering the ionic strength) is a mechanism that is not fully understood yet (Mahani et al., 2015b; Tang and Morrow, 1997). This effect has been associated in the past with a reduction of the salt content of water (the so-called Low

\* Corresponding authors at: Institute of Petroleum Engineering, Heriot-Watt University, Edinburgh, UK  
E-mail address: [j.maes@hw.ac.uk](mailto:j.maes@hw.ac.uk) (J. Maes).

**Nomenclature***Variables*

$c$	concentration (mol/L)
$D$	molecular diffusivity ( $\text{m}^2/\text{s}$ )
$f$	interior force ( $\text{N}/\text{m}^3$ )
$H$	Henry constant
$I$	ionic strength (mol/L)
$J$	molecular diffusion flux ( $\text{mol}/\text{m}^2/\text{s}$ )
$K$	stability constant
$L$	characteristic length (m)
$m$	surface concentration ( $\text{mol}/\text{m}^2$ )
$p$	pressure (Pa)
$r$	bulk chemical reaction molar rate ( $\text{mol}/\text{m}^3/\text{s}$ )
$s$	surface chemical reaction molar rate ( $\text{mol}/\text{m}^2/\text{s}$ )
$T$	temperature (K)
$t$	time (s)
$U$	characteristic velocity (m/s)
$u$	velocity (m/s)
$v$	surface complex charge
$Z$	ionic charge
$\alpha$	phase volume fraction
$\Gamma$	surface sites density ( $\text{mol}/\text{m}^2$ )
$\gamma$	interfacial tension (N/m)
$\kappa$	interface curvature ( $\text{m}^{-1}$ )
$\mu$	viscosity (Pa.s)
$\psi$	surface potential (V)
$\rho$	mass density ( $\text{kg}/\text{m}^3$ )
$\sigma$	surface charge density ( $\text{C}/\text{m}^2$ )
$\theta$	contact angle

*Constants*

$F$	Faraday constant (96490 C/mol)
-----	--------------------------------

$g$	gravity constant ( $9.81 \text{ m}/\text{s}^2$ )
$R$	universal gas constant ( $8.314 \text{ J}/\text{mol}/\text{K}$ )
$\epsilon$	dielectric constant of pure water (78.41 at 25 °C)
$\epsilon_0$	vacuum permittivity ( $8.854 \times 10^{-12} \text{ C}/\text{V}/\text{m}$ )

*subscripts*

$i$	component index
$j$	phase index
$s$	surface
$s_i$	surface component index
$st$	surface tension

*Abbreviations*

25dSW	25 × diluted Sea Water
ADRE	Advection-Diffusion-Reaction Equation
CSF	Continuous Surface Force
CST	Continuous Species Transfer
EOR	Enhanced Oil recovery
FW	Formation Water
HS	High Salinity
IHP	Inner Helmholtz plane
LBM	Lattice-Boltzmann Method
LSE	Low-Salinity Effect
LSF	Low-Salinity Flooding
NSE	Navier–Stokes Equations
OHP	Outer Helmholtz plane
PDI	Potential Determining Ions
PNM	Pore Network Modelling
PV	Pore Volume
SCM	Surface Complexation Modelling
SSF	Sharp Surface Force
SW	Sea Water
VOF	Volume-Of-Fluid

Salinity Effect, or LSE) (Tang and Morrow, 1997). However, recent advances in experimental work, in particular in the domain of fluid visualisation, greatly improved the understanding of this phenomenon.

For sandstones, Tang and Morrow (1997) observed that LSE is linked to the presence of clay minerals, and also depends on a number of factors such as oil composition, formation water composition and salinity of the injected water. A number of potential low-salinity mechanisms have been proposed in the literature such as fines migration (Tang and Morrow, 1999), interfacial tension reduction and emulsification (McGuire et al., 2005), selective plugging via clay swelling (Zhang and Morrow, 2006) and wettability alteration by multi-component ionic exchange (Tang and Morrow, 2002) and/or electrical double-layer expansion (Austad et al., 2010). Berg et al. (2010) directly visualised detachment of crude oil from clay minerals. They observed a release of crude oil when changing the brine from high to low salinity even when the amount of clay swelling was insignificant.

For carbonate rocks, the effect cannot be related to the presence of clay, as most of these rocks do not contain any, and if they do, they occur only at very low levels. Moreover, the exact chemical composition of the injected water seems to play a more important role than just salinity and ionic strength (Zhang et al., 2007). Mahani et al. (2015b) observed a LSE on calcite patches in the absence of dissolution and with an increase of interfacial tension. They could link the change of contact angle to a change of  $\zeta$ -potential, defined as the local electrical potential at the slipping plane (shear plane) that separates the stationary and mobile phases in tangential flow of the liquid with respect to the surface (Hunter, 1981). More recently, Jackson et al. (2016a); 2016b) observed that the increase of oil recovery from carbonate core-plugs obtained by

manipulating the injected water composition depends greatly on the sign of the  $\zeta$ -potential at both water/mineral and water/oil interfaces. Both these studies suggest that LSE in carbonate rocks is driven by a wettability change induced by a change of surface charge and the double-layer expansion. To analyse this effect further, Surface Complexation Models (SCM) (Goldberg, 2013) can provide a link between the water composition and the change of potential.

SCM are chemical models that provide a molecular description of adsorption phenomena using an equilibrium approach. One of the major advancements of SCM is that it considers the charges on both the adsorbing ion and the solid adsorbent surface (Goldberg, 2013). Hence, SCM can provide the link between water composition and change of surface potential. SCM for clay minerals (Bradbury and Baeyens, 1997), calcite and dolomite (Pokrovsky et al., 2000) have been proposed. In the context of EOR, Brady and Krumhansl (2012) and Brady et al. (2012) have used such models to investigate reactions at the water/oil and water/mineral interfaces that lead to oil adhesion on mineral surfaces. More recently, Mahani et al. (2016) developed a calcite SCM, adapted from Pokrovsky et al. (2000), and modified so that it can explain the impact of sulphate concentration on the  $\zeta$ -potential at the water/calcite interface.

The objective of this work is to develop an internally consistent pore-scale numerical model that (1) captures the effect of surface complexation on the surface potential and wettability of carbonate rocks, (2) can explain experimental observations at the micro-scale and (3) can be easily parameterized to study the impact of different water, mineral and oil compositions. For this, we use direct numerical simulation of the Navier–Stokes Equations (NSE) (Patankar and

Spalding, 1972) to simulate the flow. The phase distribution is solved using the Volume-Of-Fluid (VOF) method (Hirt and Nichols, 1981). The transport of chemical species is given by a pore-scale ADRE and the concentration discontinuity at the fluid/fluid interface due to thermodynamic dissolution equilibrium is treated using the Continuous Species Transfer (CST) method (Deising et al., 2016; Haroun et al., 2010). SCM is used to relate the adsorption of the Potential Determining Ions (PDI) to the change of surface potential (Mahani et al., 2016). Two simplified models that can be fitted with experimental data are proposed to relate surface potential to a change of contact angle. We then present several applications that (1) show convergence of our numerical method and concordance with experimental results, (2) allow us to perform a sensitivity analysis with respect to several parameters and production scenarios on 2D micro-models and (3) offer new physical insights into LSE.

## 2. Flow and reactive transport solvers

Three different approaches have been previously applied to solve multiphase flow problems at the pore-scale: Pore-Network Models (PNM) (Blunt and King, 1991), Lattice-Boltzmann Method (LBM) (Pan et al., 2004) and Direct Numerical Simulation (DNS) (Patankar and Spalding, 1972) of the NSE. PNM are computationally efficient but are based on simplified idealised geometries of the pore surface, which may impact modelling dynamic wettability changes. Moreover standard PNM are quasi-static, which limits their predictive capability, especially for complex recovery processes where wettability changes dynamically. Dynamic pore-network models have appeared recently (Joekar-Niasar et al., 2010; Nordhaug et al., 2003), but are generally based on adding a notional time-dependency to the invasion-percolation mechanism determined by flow rates obtained from solving the quasi-static problem. Moreover, reactive transport models based on PNM usually assume full mixing in pore bodies and throats.

LBM is based on the discrete Boltzmann equations which describes the fluids in terms of the movement and collisions of a set of particles. LBM does not require solving an implicit pressure equation, and therefore can be easily parallelized. However, LBM cannot accommodate additional physical effects such as wall-slip and dynamic contact angles easily, and has difficulties handling large viscosity and density ratios (Meakin and Tartakovsky, 2009).

DNS methods can either be mesh-free, like the smoothed particle hydrodynamics method (Tartakovsky and Meakin, 2006), or grid-based, like the finite volume method. Mesh-free methods represent sharp interface accurately and are easily parallelized. However, they are difficult to extend to reactive transport as they do not solve for concentration of species in the domain. In this work, we hence choose to use grid-based DNS with the VOF method (Hirt and Nichols, 1981).

### 2.1. The Volume-Of-Fluid method

In the VOF method, the interface between two fluids is tracked using an indicator function  $\alpha$ , which represents the volume fraction of one of the fluid in each grid cell. If the cell is completely filled with the first fluid, then  $\alpha = 1$  and if it is filled with the second fluid, then  $\alpha = 0$ . For cells which are crossed by the interface,  $\alpha$  lies between 0 and 1. The density and viscosity of the fluid are deduced by linear interpolation from the indicator function

$$\begin{aligned}\rho &= \alpha\rho_1 + (1 - \alpha)\rho_2 \\ \mu &= \alpha\mu_1 + (1 - \alpha)\mu_2,\end{aligned}\quad (1)$$

where  $\rho_i$  and  $\mu_i$  are the density and viscosity of phase  $i$ , respectively. The single-field velocity  $\mathbf{u}$  is defined as

$$\mathbf{u} = \alpha\mathbf{u}_1 + (1 - \alpha)\mathbf{u}_2, \quad (2)$$

where  $\mathbf{u}_i$  is the velocity of phase  $i$ . The NSE can be written with the

single-field formalism (Hirt and Nichols, 1981)

$$\begin{aligned}\nabla \cdot \mathbf{u} &= 0, \\ \rho \left( \frac{\partial \mathbf{u}}{\partial t} + \mathbf{u} \cdot \nabla \mathbf{u} \right) &= -\nabla p + \nabla \cdot \boldsymbol{\tau} + \rho \mathbf{g} + \mathbf{f}_{st},\end{aligned}\quad (3)$$

where  $p$  is the pressure,  $\mathbf{g}$  is the gravity vector,  $\boldsymbol{\tau}$  is the viscous stress tensor and  $\mathbf{f}_{st}$  is the surface tension force. The viscous stress tensor can be expressed as

$$\boldsymbol{\tau} = \mu(\nabla \mathbf{u} + \nabla \mathbf{u}^T). \quad (4)$$

The Reynolds number is defined as the ratio of inertial to viscous forces

$$Re = \frac{\rho LU}{\mu}, \quad (5)$$

where  $L$  and  $U$  are the reference length and velocity in the domain, and  $\rho$  and  $\mu$  are the density and viscosity of the invading phase. The Reynolds number is used to characterise different flow regimes, such as laminar flow, where viscous forces are dominant, and turbulent flow, where inertial forces are dominant. In this work, we only consider cases where  $Re < 1$ , so that we are in the so-called creeping flow regime (Lenormand et al., 1988). The indicator function  $\alpha$  is evolved with the advection equation

$$\frac{\partial \alpha}{\partial t} + \nabla \cdot (\alpha \mathbf{u}) = 0. \quad (6)$$

VOF methods can be algebraic or geometric. Algebraic methods resolve the interface by solving a discretized form of the phase advection equation Eq. (6) on a computational mesh (Ubbink and Issa, 1999), while the geometric methods explicitly reconstruct the interface, so that the solution of the advection equation conserves the volume fraction exactly (Gerlach et al., 2006). Geometric methods do not create numerical diffusion and can achieve better precision with accurate interface reconstruction (Popinet, 2009), but the calculations can be complicated, especially for unstructured grids. Algebraic methods can be easily applied to unstructured grids as no explicit interface reconstruction is needed, but numerical diffusion can smear the interface over a large number of cells. Here, we use compression of the interface to reduce this problem (Ubbink and Issa, 1999).

The surface tension force can be modelled using the Continuum Surface Force (CSF) formulation introduced by Brackbill et al. (1992)

$$\mathbf{f}_{st} = \gamma \kappa \nabla \alpha, \quad (7)$$

where  $\gamma$  is the interfacial tension between the two fluids and  $\kappa$  the mean interface curvature, which can be computed as

$$\kappa = \nabla \cdot \mathbf{n}_{12}, \quad (8)$$

where  $\mathbf{n}_{12}$  is the interface normal vector, defined as

$$\mathbf{n}_{12} = \frac{\nabla \alpha}{\|\nabla \alpha\|}. \quad (9)$$

At the fluid/fluid/solid contact line, the interface forms with the normal to the solid surface a micro-scale contact angle  $\theta$  so that

$$\mathbf{n}_{12} = \cos \theta \mathbf{n}_s + \sin \theta \mathbf{t}_s, \quad (10)$$

where  $\mathbf{n}_s$  and  $\mathbf{t}_s$  are the normal and tangent vectors to the solid surface, respectively (Brackbill et al., 1992). The capillary number  $Ca$  is defined as the ratio of viscous to surface tension forces

$$Ca = \frac{\mu U}{\gamma}, \quad (11)$$

and describes if the system is in the viscous dominated regime  $Ca > 1$  or in the capillary dominated regime  $Ca < 1$ .

The VOF-CSF method is attractive because of its simplicity. However, Scardovelli and Zaleski (1999) reported the presence of spurious currents in the capillary dominated regime, which originate from errors in calculating the normal vector and the curvature of the

interface. To limit the spurious currents, one can apply the Sharp Surface Force (SSF) method introduced by Francois et al. (2006), where the indicator function is smoothed by a Laplacian smoother for the computation of the curvature and sharpened by a curtail function for the computation of the surface tension force. Alternatively, the Filtered Surface Force (FSF), introduced by Raeini et al. (2012), filters the components of the capillary force that are parallel to the interface. SSF and FSF reduce spurious currents considerably (Raeini et al., 2012), especially for static test cases. However, Pavuluri et al. (2017) show that spurious currents appear when simulating spontaneous imbibition in a 2D straight micro-channel with VOF-SSF and VOF-FSF at  $C_a \leq 10^{-3}$ . But they also show that these spurious currents do not affect the global dynamic of the system for  $C_a \geq 10^{-4}$ . In this work, we use SSF and a minimum capillary number  $C_a = 10^{-5}$ . Spurious currents may be present, but we assume that they do not affect the global dynamic of the system.

## 2.2. Continuous Species Transfer

During a reactive transport process, the mass of each species in the fluid changes due to transport by advection and diffusion, and due to reactions. The conservation equation satisfied by the concentration  $c_{j,i}$  of a chemical species  $j$  in phase  $i$  reads

$$\frac{\partial c_{j,i}}{\partial t} + \nabla \cdot (c_{j,i} \mathbf{u}_i) = -\nabla \cdot (\mathbf{J}_{j,i}) + r_{j,i}, \quad (12)$$

where  $\mathbf{J}_{j,i}$  is the molecular diffusion flux of  $j$  in phase  $i$  and  $r_{j,i}$  is the molar rate of creation of  $j$  in phase  $i$  by chemical reactions in the pore space (in mol/m<sup>3</sup>/s). We assume that the molecular diffusion follows Fick's law

$$\mathbf{J}_{j,i} = -D_{j,i} \nabla c_{j,i}, \quad (13)$$

where  $D_{j,i}$  is the molecular diffusivity of  $j$  in phase  $i$ . Reactions that take place at the solid/fluid boundaries such as surface adsorptions are not included in  $r_{j,i}$ . Instead, they are expressed as boundary conditions on reactive surfaces (Steeff et al., 2013)

$$D_{j,i} \nabla c_{j,i} \cdot \mathbf{n}_s = s_{j,i}, \quad (14)$$

where  $s_{j,i}$  is the molar rate of creation of  $j$  in phase  $i$  by surface adsorption/desorption reactions (in mol/m<sup>2</sup>/s) and  $\mathbf{n}_s$  is the normal to the surface of the mineral.

In the absence of phase change and chemical reactions at the fluid/fluid interface, the jump conditions are given by the continuity of fluxes and chemical potentials, the latter described here by Henry's law (Danckwerts, 1970),

$$(\mathbf{J}_{j,1} - \mathbf{J}_{j,2}) \cdot \mathbf{n}_{12} = 0, \quad (15)$$

and

$$c_{j,1} H_j = c_{j,2}, \quad (16)$$

where  $H_j$  is the Henry's coefficient for species  $j$ . Haroun et al. (2010) and Marschall et al. (2012) developed the CST method to model the interface species transfer within the VOF method by defining the global variable

$$c_j = \alpha c_{j,1} + (1 - \alpha) c_{j,2}. \quad (17)$$

The global concentration ADRE is given by

$$\frac{\partial c_j}{\partial t} + \nabla \cdot (c_j \mathbf{u}) = -\nabla \cdot \mathbf{J}_j + r_j, \quad (18)$$

where

$$\begin{aligned} \mathbf{J}_j &= -(\alpha_1 D_{j,1} \nabla c_{j,1} + \alpha_2 D_{j,2} \nabla c_{j,2}), \\ r_j &= \alpha_1 r_{j,1} + \alpha_2 r_{j,2}. \end{aligned} \quad (19)$$

Haroun et al. (2010) shows that the diffusion flux  $\mathbf{J}_j$  can be written as

$$\mathbf{J}_j = -(\hat{D}_j \nabla c_j + \Phi_j), \quad (20)$$

where

$$\begin{aligned} \hat{D}_j &= \frac{1}{\frac{\alpha_1}{D_{j,1}} + \frac{\alpha_2}{D_{j,2}}}, \\ \Phi_j &= -\hat{D}_j \frac{1 - H_j}{\alpha_1 + H_j \alpha_2} c_j \nabla \alpha_1. \end{aligned} \quad (21)$$

Here  $\hat{D}_j$  is the harmonic interpolation of the phase diffusion coefficient. Haroun et al. (2010) and Deising et al. (2016) have demonstrated that this formulation is more robust than a simple mixing rule. The additional flux  $\Phi_j$  is the CST flux, which results from the concentration jump at the interface.

Finally, Graveleau (2016) derived the boundary conditions for the global concentration at the solid walls in case of a moving contact line in the absence of surface reaction. This can be adapted to include surface reactions

$$(\hat{D}_j \nabla c_j + \Phi_j) \cdot \mathbf{n}_s = s_j, \quad (22)$$

where the global surface reactions rate  $s_j$  writes

$$s_j = \alpha_1 s_{j,1} + \alpha_2 s_{j,2}. \quad (23)$$

The flow regime is described by the Péclet number, which is equal to the ratio of convection to diffusion rate

$$P_{ej} = \frac{LU}{D_j}, \quad (24)$$

where  $L$  and  $U$  are the reference length and velocity, respectively, and  $D_j$  is the diffusion coefficient of species  $j$  in the invading phase. The system is in the convection dominated regime for species  $j$  when  $P_{ej} > 1$  and in the diffusion dominated regime when  $P_{ej} < 1$ .

## 2.3. Surface complexation

In this work, we consider two different types of minerals: calcite and clay. For calcite, we use the SCM developed by Mahani et al. (2016). The rock surface presents two hydrolysis species  $> \text{CO}_3\text{H}^0$  and  $> \text{CaOH}^0$  (where  $>$  represents the mineral surface). The following species are assumed to form on the calcium and carbonate sites exposed to an aqueous solution:  $> \text{CO}_3^-$ ,  $> \text{CO}_3\text{Ca}^+$ ,  $> \text{CO}_3\text{Mg}^+$ ,  $> \text{CaO}^-$ ,  $> \text{CaCO}_3^-$ ,  $> \text{CaHCO}_3^0$  and  $> \text{CaSO}_4^-$ . We assume that the surface density  $\Gamma$  of  $> \text{Ca}$  sites and  $> \text{CO}_3$  sites are both equal to  $8.27 \mu\text{mol}/\text{m}^2$  (Pokrovsky et al., 2000). The surface-complexation reactions are summarised in Table 1.

For clay patches, we use the Na-montmorillonite SCM proposed by Bradbury and Baeyens (1997), summarised in Table 2. The surface density  $\Gamma$  of adsorption sites  $> \text{S}$  is equal to  $2.4 \mu\text{mol}/\text{m}^2$ .

For simplification, we assume that all reactions occur only on the calcite mineral surface (often termed 0-plane) and that charge and potential can be determined using a simple double-layer model (Goldberg, 2013). The total surface charge  $\sigma_s$  can be obtained by adding up the charge of all surface complex

**Table 1**

Surface-complexation reactions and their intrinsic stability constant on a calcite surface (Mahani et al., 2016).

No	Surface reactions	$\text{p}K_{\text{int}}$ at 25 °C
1	$> \text{CO}_3\text{H}^0 \rightleftharpoons > \text{CO}_3^- + \text{H}^+$	5.1
2	$> \text{CO}_3\text{H}^0 + \text{Ca}^{2+} \rightleftharpoons > \text{CO}_3\text{Ca}^+ + \text{H}^+$	1.7
3	$> \text{CO}_3\text{H}^0 + \text{Mg}^{2+} \rightleftharpoons > \text{CO}_3\text{Mg}^+ + \text{H}^+$	2.0
4	$> \text{CaOH}^0 \rightleftharpoons > \text{CaO}^- + \text{H}^+$	17
5	$> \text{CaOH}^0 + \text{CO}_3^{2-} \rightleftharpoons > \text{CaCO}_3^- + \text{OH}^-$	-1.55
6	$> \text{CaOH}^0 + \text{CO}_3^{2-} + 2\text{H}^+ \rightleftharpoons > \text{CaHCO}_3^0 + \text{H}_2\text{O}$	-22.15
7	$> \text{CaOH}^0 + \text{SO}_4^{2-} \rightleftharpoons > \text{CaSO}_4^- + \text{OH}^-$	0.1



**Table 2**

Surface-complexation reactions and their intrinsic stability constant on a clay surface (Bradbury and Baeyens, 1997).

No	Surface reactions	$pK_{int}$ at 25 °C
1	$>SOH^0 + H^+ \rightleftharpoons >SOH_2^+$	− 4.5
2	$>SOH^0 \rightleftharpoons >SO^- + H^+$	7.9
3	$>SOH^0 + Ca^{2+} \rightleftharpoons >SOCa^+ + H^+$	5.9

$$\sigma_s = F \sum_i m_{si} v_{si}, \quad (25)$$

where  $m_{si}$  and  $v_{si}$  are the surface concentration and the charge of the complex  $si$ , respectively, and  $F$  is the Faraday constant. The double-layer surface potential  $\psi_s$  is related to the surface charge by the Grahame equation (Israelachvili, 1985)

$$\sigma_s^2 = 8000\epsilon\epsilon_0 RT I \left[ \sinh\left(\frac{F\psi_s}{2RT}\right) \right]^2, \quad (26)$$

where  $\epsilon$  is the dielectric constant of pure water,  $\epsilon_0$  is the vacuum permittivity,  $I$  is the ionic strength of the electrolyte solution,  $R$  is the ideal gas constant and  $T$  is the temperature. Since charged ions are attracted to or repelled from the solid surface due to Coulomb interactions, the apparent stability constant  $K$  is different from the intrinsic one  $K_{int}$ . The relationship between the two is given by Israelachvili (1985)

$$K = K_{int} \exp\left(-\frac{Z_c F \psi_s}{RT}\right), \quad (27)$$

where  $Z_c$  is the net change of surface charge induced by the reaction (for example, − 1 for reaction 1 in Table 1). The reaction rates  $r_{j,i}$  (Eq. (12)) and  $s_{j,i}$  (Eq. (14)) are obtained by equilibrating the chemical model (Table 1 or 2) with the double-layer model (Eqs. (25)–(27)).

#### 2.4. Contact angle alteration

It has been observed in experimental work (Mahani et al., 2015a; 2015b; 2017) that the surface of a sandstone or a carbonate rock becomes less oil-wet when switching from high-salinity to low-salinity water. For example, Mahani et al. (2015a) found a change of contact angle  $\Delta\theta = 10 - 40^\circ$  for an oil droplet on a clay patch when switching from a high-salinity brine to a low-salinity brine obtained by diluting the initial brine 4, 8 or 16 times.

Mahani et al. (2015b) also found a change of contact angle  $\Delta\theta = 5 - 20^\circ$  on limestone patches and  $\Delta\theta = 0 - 45^\circ$  on dolomite patches when switching from a high-salinity Formation Water (FW) to Sea Water (SW) or 25 times diluted Sea Water (25dSW). These water compositions are given in Table 3. In the study of Mahani et al. (2015b),  $\zeta$ -potentials at the water/oil and at the water/rock interfaces were also measured. The water/oil  $\zeta$ -potential was observed to be negative and decreasing from FW to SW and 25dSW. For limestone particles, the water/rock  $\zeta$ -potential was observed to be positive for FW but negative for SW and 25dSW; a contact angle reduction was also observed. For dolomite particles, the  $\zeta$ -potential remained positive for all three water compositions. Contact angle reduction was observed for SW but not for 25dSW. To explain these changes of contact angle, it was proposed that the change of  $\zeta$ -potential from positive to negative modifies the electrostatic forces between the oil molecule and the water/rock interface from adhesive to repulsive (Brady and Krumhansl, 2012; Buckley et al., 1989). This would explain why no contact angle reduction was observed on dolomite particles for 25dSW. The change of contact angle for SW on dolomite patches could be further explained by an increase of the separation distance between oil and dolomite due to the large concentration of  $SO_4^{2-}$  (Mahani et al., 2015b).

In our simplified SCM, we assume that all surface reactions occur on the 0-plane (Fig. 1). This implies that the  $\zeta$ -potential and the potential

at the surface of the calcite are equal. In reality, only protonation and deprotonation reactions (e.g. reactions 1 and 4 in Table 1) occur on the 0-plane. For example, in a basic Stern model (Fig. 1), a layer of constant capacitance (the Stern layer) separates the mineral surface from the diffuse layer, and reactions other than protonation and deprotonation (e.g. reactions 2, 3, 5, 6 and 7 in Table 1) occur on the inner or outer planes of the Stern layer, also called Inner Helmholtz Plane (IHP) and Outer Helmholtz plane (OHP) (Al-Mahrouqi et al., 2017). Therefore, the  $\zeta$ -potential and the 0-plane potential can differ greatly. Since the reactions involving divalent ions occur on the IHP and OHP-planes, the  $\zeta$ -potential would be more accurately approximated by the OHP potential. Unfortunately, the geochemical simulator used in our numerical model (Phreeqc, see Section 2.5) does not include basic Stern model. Hence, we are using instead a simple double-layer model (Fig. 1a).

Fig. 2 shows a comparison between the  $\zeta$ -potential at a water/calcite interface, experimentally obtained by Heberling et al. (2011) and Mahani et al. (2016), and the surface potential computed using the SCM (Table 1) with a simple double-layer model. The different water compositions are represented in term of the concentration of potential determining ions  $Ca^{+2}$ ,  $Mg^{+2}$  and  $SO_4^{2-}$ .

We observe that the double-layer surface potential  $\psi_s$  only matches the trend of the  $\zeta$ -potential. Nevertheless, a simple model that describes the variation of contact angle change with  $\psi_s$  can be used to study the link between flow and wettability change induced by surface complexation, and provide new insights into the process of wettability change by surface complexation.

In the absence of robust quantitative experimental data that links surface potential to contact angle variation, two simple models are considered in this work. In the first model, we assume that the contact angle changes linearly with the surface potential

$$\theta = f_L(\psi_s) = \theta_0 + (\psi_s - \psi_0) \frac{\theta_1 - \theta_0}{\psi_1 - \psi_0}. \quad (28)$$

This model can be easily fitted to contact angle measurements and can be easily extended to piecewise linear functions, so that the function can be fitted with a large number of experimental measurements. However, this model cannot explain why 25dSW does not always induce more contact angle changes than SW. The second model considered here used a Heaviside function (Watson et al., 2017) with a critical surface potential, assumed to be equal to 0 for simplification.

$$\theta = f_H(\psi_s) = \begin{cases} \theta_0 & \psi_s > 0, \\ \theta_0 - \Delta\theta & \psi_s \leq 0. \end{cases} \quad (29)$$

The first model (Eq. (28)) is used in all applications in this study. The second model (Eq. (29)) is used in Section 3.4 to conducting a sensitivity analysis with respect to the contact angle model.

**Table 3**

Chemical composition of High Salinity (HS) brine, Formation Water (FW), Sea Water (SW) and 25 times dilute Sea Water (25dSW) ((Mahani et al., 2015a; 2016)).

	HS	FW	SW	25dSW
Na <sup>+</sup> (mg/L)	4268	49,898	13,404	536
K <sup>+</sup> (mg/L)	7237	0	483	19
Mg <sup>+2</sup> (mg/L)	23.20	3248	1618	65
Ca <sup>+2</sup> (mg/L)	301.6	14,501	508	20
Sr <sup>+2</sup> (mg/L)	0	0	17	1
Cl <sup>−</sup> (mg/L)	13,746	111,812	24,141	967
SO <sub>4</sub> <sup>2−</sup> (mg/L)	0	234	3384	135
HCO <sub>3</sub> <sup>−</sup> (mg/L)	0	162	176	7
Ionic strength (mol/L)	0.40	3.67	0.87	0.035
pH	7	6.9	8.0	7.4
Density (kg/m <sup>3</sup> )	1015	1121	1034	998
Viscosity (mPa.s)	1.0	1.1	1.0	1.0

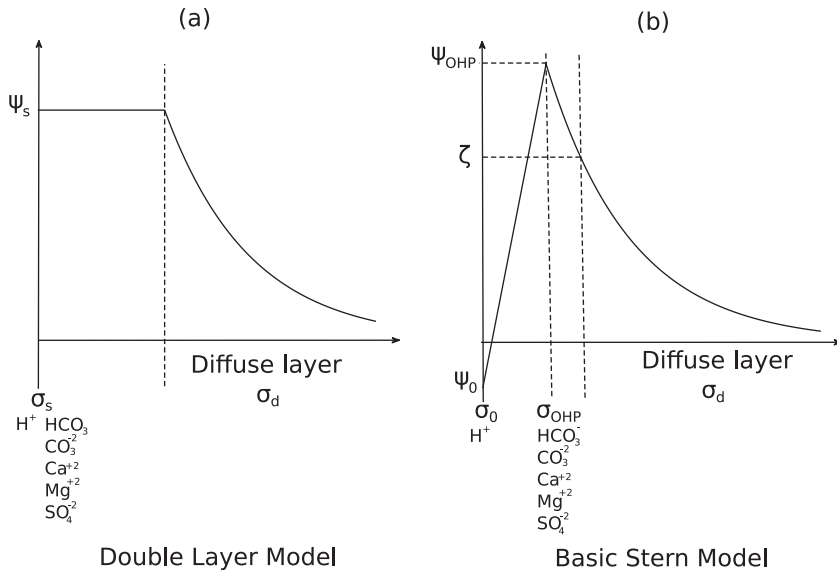


Fig. 1. A schematic representation of the electric double-layer model used in this study (a) and a basic Stern model (b).

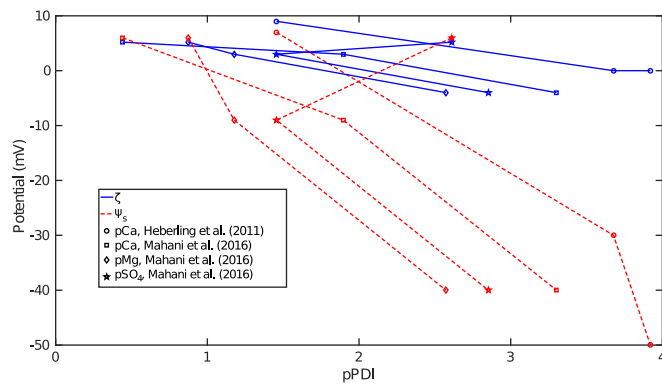


Fig. 2. Evolution of the  $\zeta$ -potential at a water/calcite interface obtained experimentally (solid lines), and the surface potential  $\psi_s$  computed using the surface complexation model in Table 1 with a simple double-layer model (dashed lines), with respect to concentration of potential determining ions  $\text{Ca}^{+2}$ ,  $\text{Mg}^{+2}$  and  $\text{SO}_4^{-2}$ . The data marked in circles are obtained from Heberling et al. (2011) and the data marked in squares, diamonds and pentagrams are obtained from Mahani et al. (2016). We observe that  $\psi_s$  only matches the trend of  $\zeta$ , and that for the water compositions considered here, the potentials were not related to the concentration of sulphate ions.

## 2.5. Numerical implementation

The mathematical model given by the NSE (Eq. (3)) and the phase advection equation (Eq. (6)) is implemented in the open source computational fluids dynamics software OpenFOAM ([www.OpenFOAM.org](http://www.OpenFOAM.org)) as an internal VOF solver, so-called *interFoam*. *interFoam* solves the NSE on a collocated Eulerian grid with a predictor-corrector strategy based on the Pressure Implicit Splitting Operator (PISO) algorithm (Issa et al., 1985). An explicit formulation is used to treat the coupling between the phase distribution equation (Eq. (6)) and the NSE. This imposes a limit on the time-step size by introducing a capillary wave time-scale described by the Brackbill conditions (Brackbill et al., 1992). In all simulations, we use a constant time-step that satisfies this condition. Time discretization is performed using the Crank–Nicolson scheme, and space discretization is performed using the second-order van Leer scheme (van Leer, 1974).

For the purpose of this work, we extended the *interFoam* solver to perform two-phase reactive transport simulations. The concentration equation (Eq. (18)) is solved sequentially after the phase conservation equation (Eq. (6)). Time discretization is again based on the Crank–Nicolson scheme. The advection term  $\nabla \cdot (cu)$  and the CST flux  $\Phi$  space

discretization is again based on the second-order van Leer scheme (van Leer, 1974). The diffusion term  $\nabla \cdot (D_j \nabla c_j)$  is discretized using the Gauss linear limited corrected scheme, which is second order and conservative. All of these discretization schemes are available in the standard OpenFOAM distribution.

The surface complexation model (Eqs. (25)–(27)) is solved using the US Geological Survey chemical package Phreeqc ([www.usgs.gov/software/phreeqc](http://www.usgs.gov/software/phreeqc)). The coupling between transport and reactions is handled by a sequential split operator method (Carrayrou et al., 2004). First, the transport step solves the system of equations in the absence of chemical reactions using OpenFOAM. Then, the reaction step solves the system in the absence of flow using Phreeqc. For this, the concentration boundary condition on a reactive surface (Eq. (22)) is integrated over a control volume and gives an additional source term in the ADRE (Eq. (18)).

Our numerical model was validated by comparison with analytical solutions for spontaneous imbibition in a 2D rectangular channel (Pavuluri et al., 2017), for steady-state interface mass transfer in a 2D tube (Graveleau, 2016) and for linear retardation in a 1D semi-infinite column (Ogata and Banks, 1961). For each case, the numerical solution was shown to converge toward the analytical solution and a relative error below to 1% was obtained for sufficient resolution. Additional convergence tests are shown in Section 3.3.

## 3. Applications

We present five applications of our numerical model. First, we consider a batch experiment investigating the equilibrium between calcite and water for different water compositions, and the corresponding change of surface potential. Secondly, we simulate the detachment of an oil droplet from a clay patch and compare 3D simulations with experimental results (Mahani et al., 2015a). Thirdly, we study the convergence of the numerical model and the final residual oil saturation for the invasion of an idealised 2D square-shaped pore by different types of water. Fourthly, we consider a simple  $3 \times 3$  heterogeneous calcite micro-model in order to perform a sensitivity analysis with respect to several parameters of the model. Finally, we simulate water invasion in a complex 2D porous media and study different production scenarios. For all 2D applications, gravity is ignored.

The fluids used are water and oil. We used four different water compositions (Table 3) that have been used previously in experimental studies: High Salinity (HS) brine, obtained by dissolving pure salts NaCl, KCl,  $\text{CaCl}_2 \cdot \text{H}_2\text{O}$  and  $\text{CaCl}_2 \cdot \text{H}_2\text{O}$  into pure water (Mahani et al.,

2015a), Formation Water (FW) from a Middle Eastern carbonate field, Sea Water (SW) and 25 times diluted Sea Water (25dSW) (Mahani et al., 2016).

The diffusion coefficients of ions in water are obtained from Li and Gregory (1973) and are summarised in Table 4. The initial concentration of ions in the oil phase is zero, and the Henry constant of every ions is assumed to be 0 too, so that there is no ion transfer between the phases. The oil density and viscosity are equal to 840 kg/m<sup>3</sup> and 6.5 mPa.s (North Sea crude oil from Mahani et al. (2015a)), respectively. The interfacial tension is equal to 10 mN/m.

### 3.1. Decomposition of low-salinity effect on calcite

As mentioned previously, LSE is a mechanism that is still not well understood and more studies are necessary to capture the driving factors and predict an increase in oil recovery. In this example, we use SCM to decompose the LSE on calcite. Mahani et al. (2016) studied the effect of pH on the surface potential. However, as it has been noted by Alroudhani et al. (2016) and Jackson et al. (2016a), a modification of the pH would change the dissolution equilibrium between calcite and water, and can greatly affect the concentration of Ca<sup>2+</sup> in the water. Instead, these studies analysed the evolution of surface potential with the concentration of PDIs.

Using the SCM defined in Table 1, we identify three mechanisms responsible for lowering the surface potential of the calcite when switching from FW to 25dSW:

- Desorption of Ca<sup>2+</sup> and Mg<sup>2+</sup>. These ions are in competition with H<sup>+</sup> for a > CO<sub>3</sub> surface site. Lower concentration of the divalent ions generates more sorption of the monovalent ion, therefore lowering the positive part of the surface charge.
- Sorption of SO<sub>4</sub><sup>2-</sup> and desorption of HCO<sub>3</sub><sup>-</sup>. These ions are in competition with OH<sup>-</sup> for a > Ca surface site. Lower concentration of the monovalent ions generates more sorption of the divalent ion, therefore increasing the negative part of the surface charge.
- Lowering the concentration of surface-inert ions (Na<sup>+</sup>, K<sup>+</sup>, Sr<sup>2+</sup> and Cl<sup>-</sup>) in solution. This affects the surface potential by lowering the ionic strength of the solution.

We perform three simulations in Phreeqc which represents batch experiments to study the effect of each mechanism. First, we lower the concentration of Ca<sup>2+</sup> and Mg<sup>2+</sup> in solution while keeping the other concentrations constant. Then, we lower the concentration of SO<sub>4</sub><sup>2-</sup> and HCO<sub>3</sub><sup>-</sup>. Finally, we lower the concentration of Na<sup>+</sup>, K<sup>+</sup>, Sr<sup>2+</sup> and Cl<sup>-</sup> (A → B → C). Then, we change the order of the steps (B → C → A and C → A → B). Fig. 3 shows the evolution of surface potential with ionic strength during each step for each simulation.

We observe that in each case, step (A) has the most impact on the surface potential. The average change of surface potential is -40 mV. This is because FW has a very high initial concentration of Ca<sup>2+</sup> and Mg<sup>2+</sup>. Initially, every > CO<sub>3</sub> site is occupied by a divalent ion. Lowering the concentration of these ions has therefore a major impact on the surface charge. Step (B) has a smaller impact on the surface potential. The average change of surface potential is - 8 mV. Note that here, we lower the concentration of the divalent ion SO<sub>4</sub><sup>2-</sup>, which by itself should increase the surface charge, but we also lower the concentration of HCO<sub>3</sub><sup>-</sup>, so that the relative concentration of divalent ions actually increases, and the surface charge decreases. The effect is less important than step (A), since the initial concentration of SO<sub>4</sub><sup>2-</sup> is large enough so that most of > Ca sites are initially occupied by a divalent ion. Finally, we observe that step (C) can have either a positive or a negative impact on the surface potential. Indeed, step (C) only marginally changes the surface adsorption as it only affects the ionic strength. Therefore, it does not change the sign of the surface potential, only the magnitude. Indeed, when we perform step (C) first, the surface potential actually increases from 7 to 8.5 mV.

This analysis shows that the surface potential is more affected by the chemical composition of the water than by its salinity. It also suggests that the driving mechanism of the LSE on calcite is the desorption of Ca<sup>2+</sup> and Mg<sup>2+</sup> ions. The effect of other ions, in particular sulphate and bicarbonate, depends strongly on the composition of the formation water. This confirms the trends observed in Fig. 2. Mineralogy could also have a large impact (e.g. presence of dolomite).

### 3.2. Oil droplet detachment from a clay patch

In this section, we consider an oil droplet on a clay patch. The system is equilibrated first under high-salinity brine (HS, Table 3), before switching to a low-salinity brine, obtained by diluted HS 4 times. The HS equilibration lasted 72 h, and we focused here on the second part of the experiment.

The volume of the droplet is equal to 3.1 mm<sup>3</sup>. At equilibrium with HS, the contact angle  $\theta$  is equal to 55° and the initial contact area is equal to 1.1 mm<sup>2</sup>. The surface potentials, computed with Phreeqc, are equal to -7.3 mV when equilibrated with HS and -15.6 mV with the 4 times diluted brine. The contact angle variation is modelled using a linear function (Eq. (28)), fitted to experimental data from Mahani et al. (2015a) for the initial contact angle and the contact angle at detachment (Fig. 4).

We use a uniform 3D Cartesian grid with  $\Delta x = \Delta y = \Delta z = 0.05$  mm. The surface of the clay patch reacts with the low-salinity brine and calcium ions are desorbed from the surface (Eq. (14)). The excess of calcium and magnesium diffuses away from the surface of the patch and more reaction occurs. The electric potential of the solid surface decreases, and as a result, the contact angle changes and the oil droplet recedes from the surface until it detaches by buoyancy (Fig. 7).

However, Mahani et al. (2015a) observed a time-scale of detachment two order of magnitude longer than expected by diffusion only. They proposed that this discrepancy could be explained by electrostatic effects in the thin film than forms near the charged clay surface. Fig. 5 shows a schematic representation of these electrostatic effects.

The variation of surface potential induces a gradient of electrostatic potential inside the thin film, opposed to the gradient of cation concentration. Therefore, the electrostatic force generates a flux opposed to the diffusion flux. This can be modelled using the Nernst-Planck equation in the thin film

$$J_j = D_j \left( \nabla c_j + \frac{Z F c_j}{R T} \nabla \psi \right). \quad (30)$$

However, this cannot be simply implemented in our model at the micro-scale because the thin film is of a few nano-meters in thickness. Instead, we include these effects by modifying the molecular diffusion near the surface. The boundary condition for the phase concentrations on a reactive surface (Eq. (14)) is replaced by

$$D_{j,i}^{NS} \nabla c_{j,i} \cdot \mathbf{n}_s = S_{j,i}, \quad (31)$$

where  $D^{NS}$  is the near-surface diffusion. Fig. 6 shows the evolution of the contact angle during the simulation for different values of  $D^{NS}$  and a comparison with experimental data presented in Mahani et al. (2015a).

First, we use  $D^{NS} = D$ , where  $D$  represents the values presented in

**Table 4**  
Diffusion coefficient of ions in water (obtained from Li and Gregory (1973)).

Ion	D (10 <sup>-9</sup> m <sup>2</sup> /s)	Ion	D (10 <sup>-9</sup> m <sup>2</sup> /s)
H <sup>+</sup>	9.83	OH <sup>-</sup>	5.27
Na <sup>+</sup>	1.33	K <sup>+</sup>	1.96
Mg <sup>2+</sup>	0.70	Ca <sup>2+</sup>	0.79
Sr <sup>2+</sup>	0.794	Cl <sup>-</sup>	2.03
HCO <sub>3</sub> <sup>-</sup>	1.18	CO <sub>3</sub> <sup>2-</sup>	0.95
SO <sub>4</sub> <sup>2-</sup>	1.07	-	-

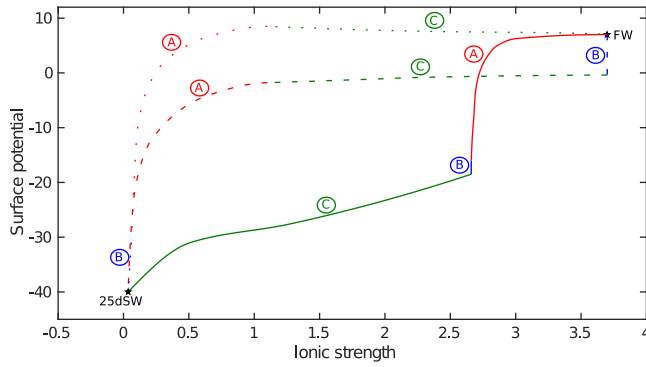


**Fig. 3.** Decomposition of low-salinity effect on calcite when replacing Formation Water (FW) by 25 times diluted Sea Water (25dSW). We consider the three mechanisms A (desorption of calcium and magnesium), B (sorption of sulphate and desorption of carbonate) and C (lowering the concentration of surface-inert ions), and study the impact of the order of the steps by performing A → B → C (solid line), B → C → A (dash line) and C → A → B (dot line). We observe that step A has the most impact and that step C can both increase or decrease the surface potential.

**Table 4.** We obtain a time of detachment of 250 s. Then, we use  $D^{NS} = \frac{D}{10}$ ,  $D^{NS} = \frac{D}{100}$  and  $D^{NS} = \frac{D}{150}$ . We observe that for  $D^{NS} = \frac{D}{150}$ , the numerical simulation matches qualitatively the experiment. Fig. 7 shows the evolution of the droplet shape with time during the simulation. We conclude that our numerical model is able to match experimental results obtained in Mahani et al. (2015a). However, there are two drawbacks of not including the thin film in the model explicitly. First, the parameters  $D^{NS}$  cannot be evaluated a-priori and need to be matched by comparison with experimental results. In test cases (3.3) and (3.5), the electrostatic effects are ignored, while in test case (3.4), the sensitivity of the recovery factor with respect to  $D^{NS}$  is explored. Secondly, Bartels et al. (2017) show that the low-salinity effect can induce oil remobilisation without buoyancy. Joekar-Niasar and Mahani (2017) show that the pressure dynamic inside the thin film can lead to expansion of the film and deformation of the fluid/fluid interface, potentially resulting in oil remobilisation. In test cases (3.3) and (3.4), the initial saturation of water is ignored, so that no oil is trapped, and the effect of pressure in the thin film can be ignored. In test case (3.5), we show that our model can simulate the increase of pore-scale sweep efficiency in response of low-salinity flooding, but not the oil remobilisation effect in the absence of buoyancy.

### 3.3. 2D square-shaped pore

In this application, we consider a single, idealised, and two-dimensional idealised pore constituting of one square connected to two

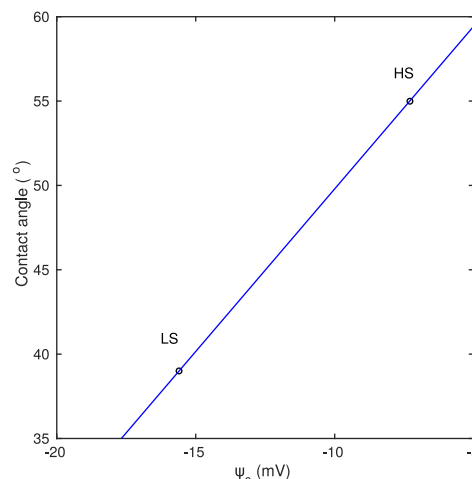
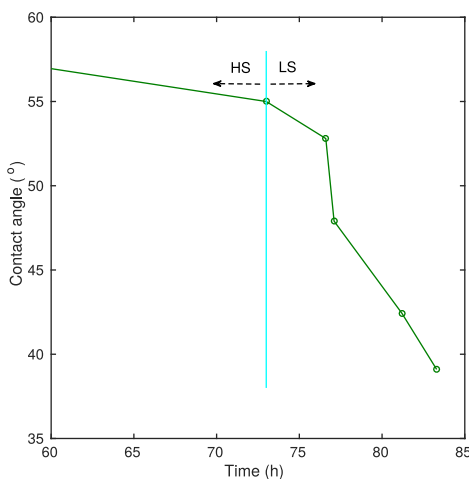


**Fig. 4.** (a) Evolution of contact angle during an experiment where an oil droplet detaches from a clay patch (Mahani et al., 2015a) and (b) numerical model representing the variation in contact angle as a function of surface potential.

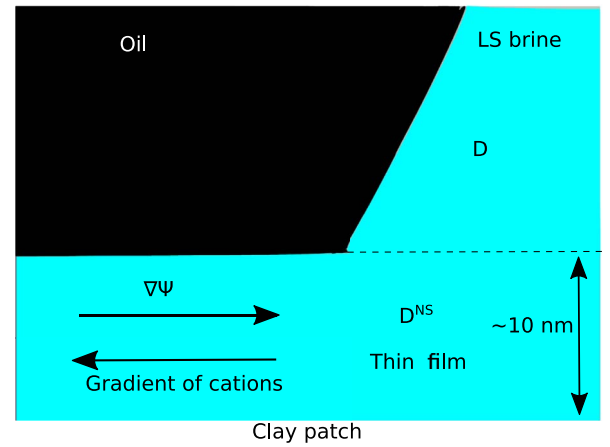


**Fig. 5.** A schematic representation of electrostatic effects near the surface of the clay patch.

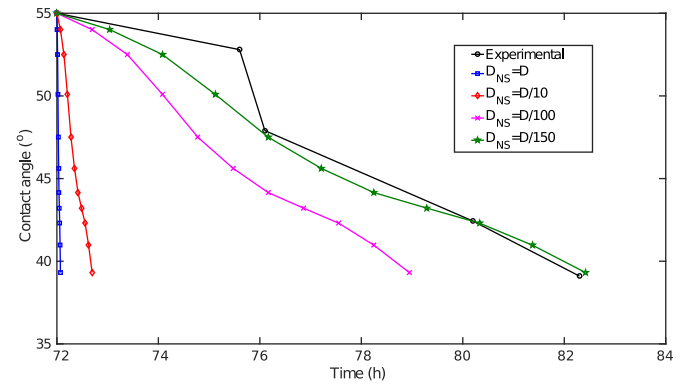


**Fig. 6.** Evolution of the contact angle during simulation of oil droplet detachment from a clay patch by low-salinity effect for different values of  $D^{NS}$  and a comparison with experimental data obtained in Mahani et al. (2015a).  $D$  represents the values presented in Table 4.

throats. We explore the convergence of the numerical model. Fig. 8 presents the geometry of the domain and the inlet and outlet boundary conditions. The pore surfaces are assumed to be calcite (Table 1). The pore space is initially filled with oil, but the surface of the pore is at equilibrium with a nano-scale thin film of FW (Table 3). The surface potential, calculated with Phreeqc, is equal to 7 mV, but the effect of the thin film on the hydrodynamics of the system is ignored ( $\alpha = 0$  and  $D^{NS} = D$ ).

At  $t = 0$  s, we inject FW, SW or 25dSW at the inlet, with a velocity of



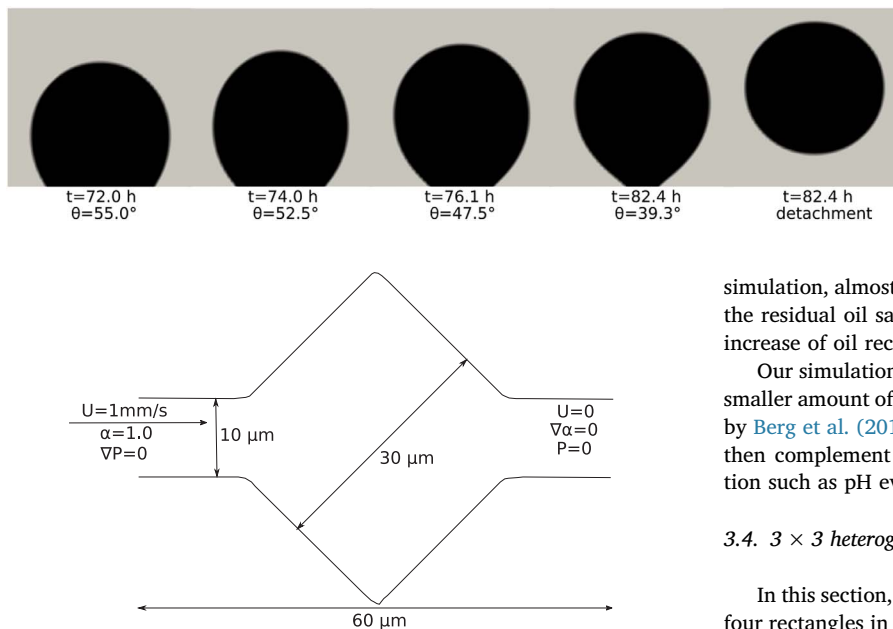


Fig. 8. Geometry and boundary conditions during water invasion in a 2D square-shaped pore. We use different grid resolution from 5  $\mu\text{m}$  to 0.5  $\mu\text{m}$  to study the convergence of the numerical model.

1 mm/s, which corresponds to a capillary number  $Ca = 10^{-4}$ . The surface potential of the calcite equilibrated with SW (respectively 25dSW) computed with Phreeqc is equal to -9 mV (respectively -40 mV). To explore convergence and sensitivity for different values of contact angles, we assume  $\theta_{FW} = 120^\circ$ ,  $\theta_{SW} = 110^\circ$  and  $\theta_{25dSW} = 90^\circ$ . This corresponds to  $\partial\theta/\partial\Psi = 0.64^\circ/\text{mV}$  (Eq. (28)).

To study grid convergence for each case (FW, SW and 25dSW), we use a fine-grid solution ( $\Delta x = \Delta y = 0.5 \mu\text{m}$ ) as a reference solution. All cells containing solids are removed and replaced by rectangular and triangular cells that match the solid boundaries. We then compare the final residual oil saturation in the domain obtained at different grid resolutions.

Fig. 9 shows the evolution of the relative error for the three cases.

We observe that the simulations have converged for a resolution of 1  $\mu\text{m}$ . Fig. 10 shows the corresponding evolution of the indicator function  $\alpha$  and the water pH during invasion with FW, SW and 25dSW. Blue corresponds to water and red to oil. The water pH during FW invasion remains constant equal to 6.9 during the simulation since calcite has been previously equilibrated with FW. At the end of the simulation, a significant fraction of oil remains at the top and bottom corner of the pore. This corresponds to a residual oil saturation  $S_{or}(FW) = 0.07$ .

During invasion with SW, the contact angle changes from  $120^\circ$  to  $110^\circ$  as calcite equilibrates with water. We observed that the pH increases from 8 to approximately 9 near the pore surface where the reactions take place. At first glance, this observation could be surprising as the calcite has been previously equilibrated with FW which has a pH of 6.9. However, we show in Section 3.1 that the most important mechanism of surface potential reduction during the replacement of FW by 25dSW is the desorption of calcium and magnesium on the pore surface. This is described by reactions 2 and 3 in Table 1. During these reactions,  $H^+$  ions are adsorbed onto the surface, effectively increasing the pH of the solution. At the end of the simulation, oil still remains at the top and bottom of the pore, but the residual oil saturation  $S_{or}(SW)$  is 0.03, which corresponds to an increase of oil recovery of 4%.

During invasion with 25dSW, the contact angle changes from  $120^\circ$  to  $90^\circ$  as the calcite equilibrates with water. More  $Ca^{+2}$  and  $Mg^{+2}$  are desorbed from the calcite and more  $H^+$  is adsorbed. The effect of surface reactions on the pH is stronger, especially near the inlet where 25dSW is in contact with calcite for the first time. At the end of the

Fig. 7. Numerical simulation of an oil droplet detachment from a clay patch induced by low-salinity. The water/oil/clay contact line reaches equilibrium after 10.4 hours and the droplet detaches. This is in good agreement with experimental data from Mahani et al. (2015a).

simulation, almost no oil remains at the top and bottom of the pore, and the residual oil saturation  $S_{or}(SW)$  is 0.0025, which corresponds to an increase of oil recovery of 6.75%.

Our simulations show that flooding by a low-salinity water leaves a smaller amount of residual oil inside a pore, as observed experimentally by Berg et al. (2010) and Chen et al. (2010). Our numerical model can then complement such experiments by providing additional information such as pH evolution.

### 3.4. $3 \times 3$ heterogeneous micro-model

In this section, we consider a 2D micro-model formed by subtracting four rectangles in a 2D square of calcite (Table 1). The resulting micro-model includes  $3 \times 3$  nodes, and is presented in Fig. 11. Similarly to the previous test case, the domain is initially filled with oil ( $\alpha = 0$ ), but the pore surfaces are at equilibrium with a nano-scale FW thin film (Table 3), so that the surface potential, computed with Phreeqc, is equal to 7 mV.

The aim of this test case is to analyse how recovery factors vary with water composition, contact angle change, injection velocity and near-surface diffusion. For this, we assume  $\theta_{FW} = 120^\circ$ ,  $\theta_{SW} = 110^\circ$  and  $\theta_{25dSW} = 90^\circ$ . First, we assume that the contact angle is a linear function of the surface potential (Eq. (28)), that the injection velocity  $U$  is equal to 1 mm/s ( $Ca = 10^{-4}$ ) and that  $D^{NS} = D$ . We perform a convergence study, similar to the one conducted in the previous application (Section 3.3) and we obtain convergence for a grid with a resolution of 1  $\mu\text{m}$ .

Fig. 12 shows the evolution of the indicator function  $\alpha$  during invasion with FW, SW and 25dSW. Blue corresponds to water and red to oil. We observe that SW invades more throats than FW, and that 25dSW invades the entire domain. This indicates an increase of pore-scale sweep efficiency with reduction of water salinity. This can also be observed in a more complex 2D pore structure, as discussed in Section 3.5 below. The residual oil saturation are  $S_{or}(FW) = 0.177$ ,  $S_{or}(SW) = 0.077$  and  $S_{or}(25dSW) = 0.001$ . These correspond to an increase of oil recovery of 10% and 17.6% for SW and 25dSW, respectively.

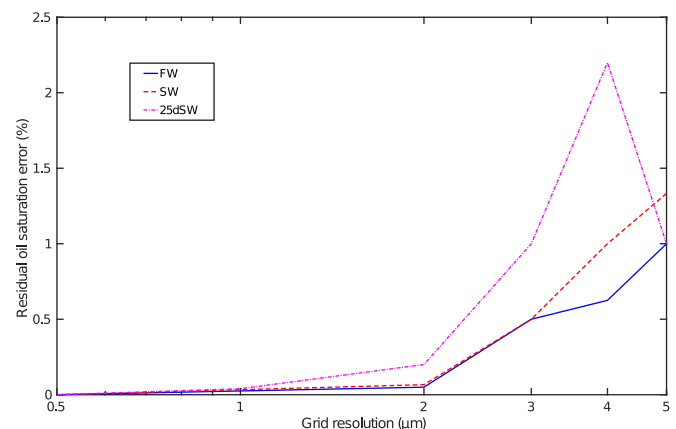
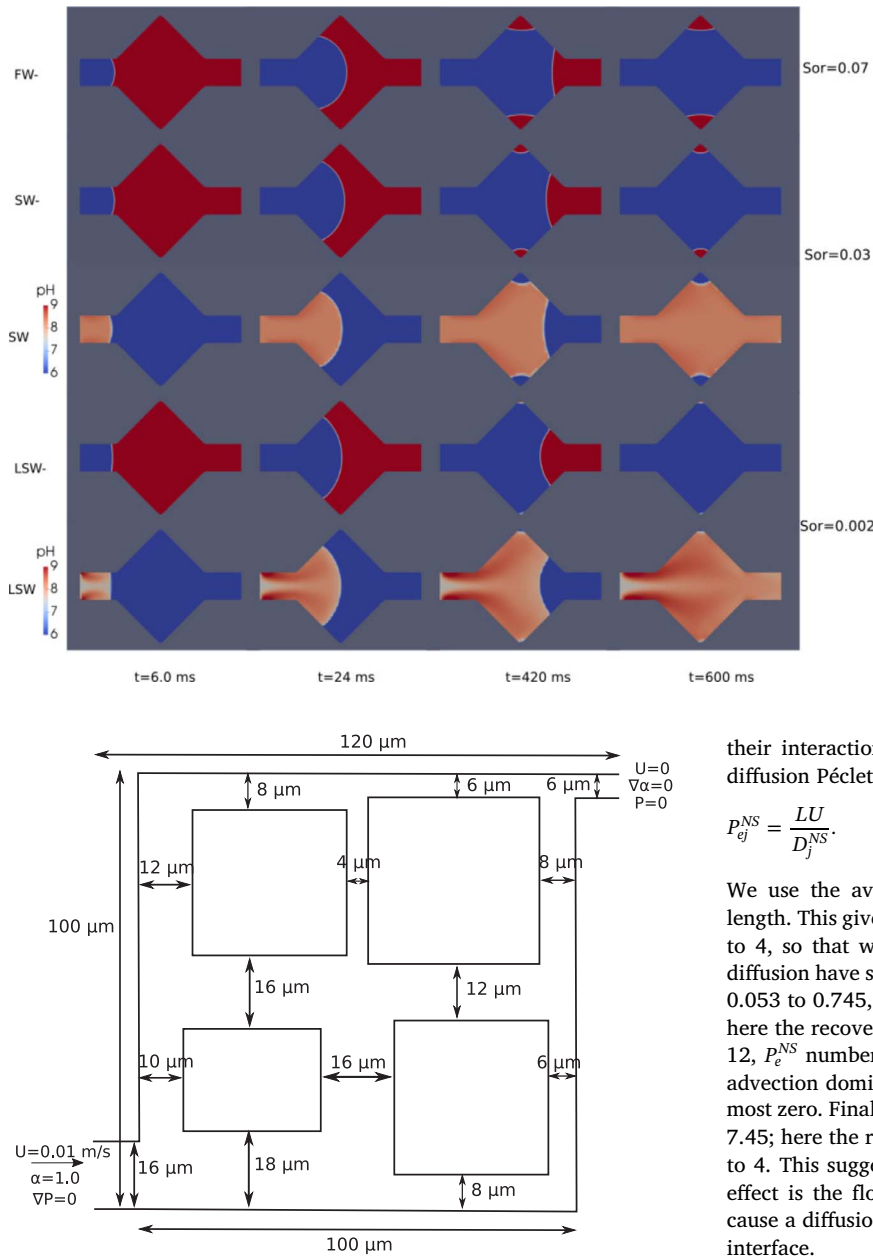


Fig. 9. Grid convergence study for water invasion in a 2D square-shaped pore (see Fig. 8 for model dimension) considering Formation Water (FW), Sea Water (SW) and 25 dilute Sea Water (25dSW). The simulations have converged for a resolution of 1  $\mu\text{m}$ .



**Fig. 10.** Evolution of the indicator function  $\alpha$  and water pH during invasion in a 2D calcite square-shaped pore during waterflooding with Formation Water (FW), Sea Water (SW) and 25 times diluted Sea Water (25dSW). Blue corresponds to water and red to oil. The pH during FW invasion remains constant and equal to 6.9. We observe less oil remaining at the corner of the pore for SW and 25dSW. The final residual oil saturation are  $S_{or}(FW) = 0.07$ ,  $S_{or}(SW) = 0.03$  and  $S_{or}(25dSW) = 0.0025$ , respectively. (For interpretation of the references to colour in this figure legend, the reader is referred to the web version of this article.)

**Fig. 11.** Geometry and boundary conditions during water invasion in a  $3 \times 3$  heterogeneous micro-model. We use a grid of resolution  $1 \mu\text{m}$ .

We then perform a sensitivity analysis considering four different parameters: water composition (described here by ionic strength  $I = 0.87$  for SW and  $I = 0.035$  for 25dSW), contact angle model (Eq. (28) or Eq. (29)), injection velocity (1 or 0.1 mm/s) and near-surface diffusion ( $D^{NS} = D$  or  $D^{NS} = D/10$ ). To perform the sensitivity analysis and compare the results, we use a two-level factorial design (Myers et al., 2009) and a measure of performance equal to the increase of recovery factor by comparison with FW injection. Table 5 shows the full summary of the sensitivity analysis. The response is then analysed using a first-order model with interactions (Myers et al., 2009). Fig. 13 shows the corresponding Pareto chart (Myers et al., 2009) showing the eight most important effects.

We observe that the most important factors are the injection velocity, the near-surface diffusion and the water composition, described here by the ionic strength  $I$ . The impact of the contact angle model is small in comparison and can be ignored as a first order approximation. We also note that an important part of the impact of  $U$  and  $D^{NS}$  is due to

their interaction. This can be expressed in term of the near surface diffusion Péclet number

$$P_{ej}^{NS} = \frac{LU}{D_j^{NS}}. \quad (32)$$

We use the average pore throat radius  $L = 5.21 \mu\text{m}$  as a reference length. This gives Péclet numbers between 0.53 and 7.45 for test cases 1 to 4, so that we are in the transitional regime where advection and diffusion have similar time-scales. For test cases 5 to 8,  $P_e^{NS}$  ranges from 0.053 to 0.745, so that we are now in the diffusion dominated regime; here the recovery factors slightly increase. However, for test cases 9 to 12,  $P_e^{NS}$  number ranges from 5.3 to 74.5. In these cases, we are in the advection dominated regime, and the increase of recovery factor is almost zero. Finally, for test cases 13 to 16,  $P_e^{NS}$  ranges again from 0.53 to 7.45; here the recovery factors are identical to the ones for test cases 1 to 4. This suggests that the most important factor for the low-salinity effect is the flow regime. Advection needs to be sufficiently slow to cause a diffusion-induced change in contact angle near the water/solid interface.

### 3.5. Complex 2D porous medium

In this test case, we consider a complex 2D porous medium representing a thin section of a real carbonate grainstone (Zaretsky et al., 2010). The pore surfaces are assumed to be calcite (Table 1). The geometry and boundary conditions are summarised in Fig. 14. The porosity and permeability of the sample have been numerically estimated to 0.4 and  $0.71 \times 10^{-12} \text{ m}^2$ , respectively.

The aim of this test case is to study three different production scenarios: FW injection, SW injection and FW injection followed by SW injection. We assume that the domain is initially filled by oil ( $\alpha = 0$ ), but the pore surfaces are at equilibrium with a nano-scale FW thin film (Table 3), so that the surface potential, computed with Phreeqc, is equal to 7 mV. The surface potential of the calcite equilibrated with SW computed with Phreeqc is equal to  $-9 \text{ mV}$ . The contact angle is assumed to be a linear function of the surface potential (Eq. (28)), fitted with experimental data for an oil droplet on a limestone plate from Mahani et al. (2015b) (Fig. 15).

The domain is represented by a 2D uniform Cartesian grid comprising  $1000 \times 500$  grid blocks. All cells containing solid are removed

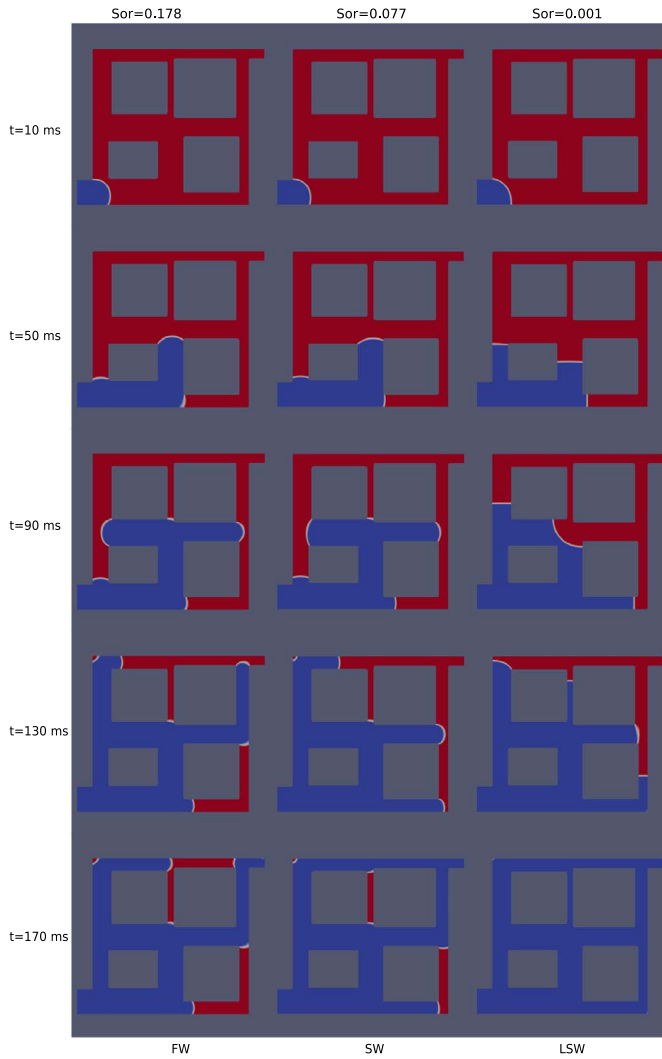


**Fig. 12.** Evolution of the indicator function  $\alpha$  in a  $3 \times 3$  calcite micro-model (see Fig. 11 for model dimension) during waterflooding with Formation Water (FW), Sea Water (SW) and 25 times diluted Sea Water (25dSW). Blue corresponds to water and red to oil. We observe that SW invades more throats than FW, and that 25dSW invades almost the entire domain. The final residual oil saturation are  $S_{or}(FW) = 0.177$ ,  $S_{or}(SW) = 0.077$  and  $S_{or}(25dSW) = 0.001$ , respectively. (For interpretation of the references to colour in this figure legend, the reader is referred to the web version of this article.)

**Table 5**

Summary of the two-level factorial sensitivity analysis for the increase of recovery factor during low-salinity flooding simulations in a  $3 \times 3$  micro-models (Fig. 11).

Trial number	$I$	$\theta$ model	$U$ (mm/s)	$D^{NS}$	Increase of recovery factor (%)
1	0.87	$f_L$	1	$D$	10
2	0.035	$f_L$	1	$D$	17.6
3	0.87	$f_H$	1	$D$	11.1
4	0.035	$f_H$	1	$D$	18.1
5	0.87	$f_L$	0.1	$D$	11.1
6	0.035	$f_L$	0.1	$D$	18.1
7	0.87	$f_H$	0.1	$D$	11.1
8	0.035	$f_H$	0.1	$D$	18.1
9	0.87	$f_L$	1	$D/10$	0.1
10	0.035	$f_L$	1	$D/10$	0.1
11	0.87	$f_H$	1	$D/10$	0.1
12	0.035	$f_H$	1	$D/10$	0.1
13	0.87	$f_L$	0.1	$D/10$	10
14	0.035	$f_L$	0.1	$D/10$	17.6
15	0.87	$f_H$	0.1	$D/10$	11.1
16	0.035	$f_H$	0.1	$D/10$	18.1

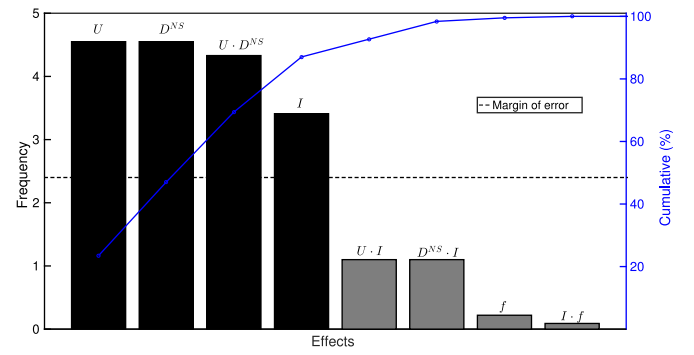


**Fig. 13.** Pareto chart of the 8 most important effects causing an increase of recovery factor by low-salinity flooding.

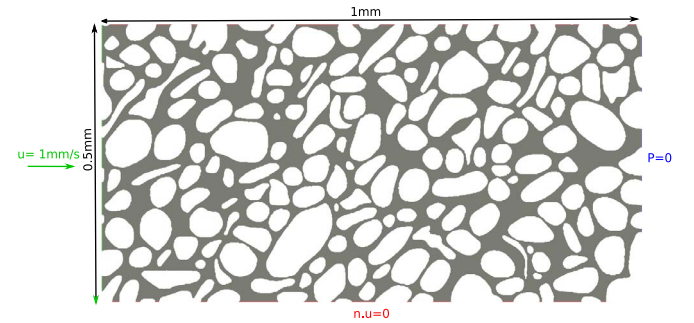


**Fig. 14.** Pore geometry and boundary conditions for water invasion in a complex 2D porous medium.

and replaced by rectangular and triangular cells that match the solid boundaries. The final grid contains 204,728 cells. Fig. 16 shows the evolution of the indicator function  $\alpha$  during FW and SW injection, at different times corresponding to 0.25, 0.5, 1 and 2 Pore Volume (PV) injected.

We observe that the overall residual oil saturation is impacted by the change of wettability in two ways. First, the water phase remains more connected during SW flooding compared to FW flooding. As a consequence, FW leaves a larger number of small clusters of oil in the pore-space after invasion. This is particularly visible in the solid rectangle shown on Fig. 16. Secondly, the invasion pattern changes and more pores are being invaded during SW flooding compared to FW flooding. This is particularly visible in the dashed rectangle shown on Fig. 16. Both these effects contribute to an increase of pore-scale sweep efficiency induced by wettability change. After 3 PV injected, the oil saturation has reached an equilibrium in both cases.

We then consider the production scenario where we inject 2 PV of FW followed by 2 PV of SW. Fig. 17 compares the final phase distributions for FW flooding only and FW flooding followed by SW flooding. We observe that the amount and form of oil clusters left in the pore space after invasion (solid rectangle on Fig. 17) remain mostly unchanged. This suggests that, even though our numerical model can simulate droplet detachment by buoyancy under LSE (Section 3.2), it is not able to simulate oil remobilisation due to LSE in the absence of buoyancy. Bartels et al. (2017) observed oil remobilisation in the absence of buoyancy in a 2D micro-model, and showed that the mechanism was driven by thin film dynamics, which we do not include in our model. However, we do observe an increase in the number of invaded pores (dashed rectangle on Fig. 17). The change of wettability reduces the capillary resistance in the domain and unlocks additional pores for the water invasion.

Fig. 18 shows the evolution of the oil saturation in the domain during FW flooding, SW flooding and FW flooding followed by SW flooding. The final oil saturations are  $S_{or}(FW) = 0.402$ ,  $S_{or}(SW) = 0.341$  and  $S_{or}(FW-SW) = 0.318$ . These correspond to an

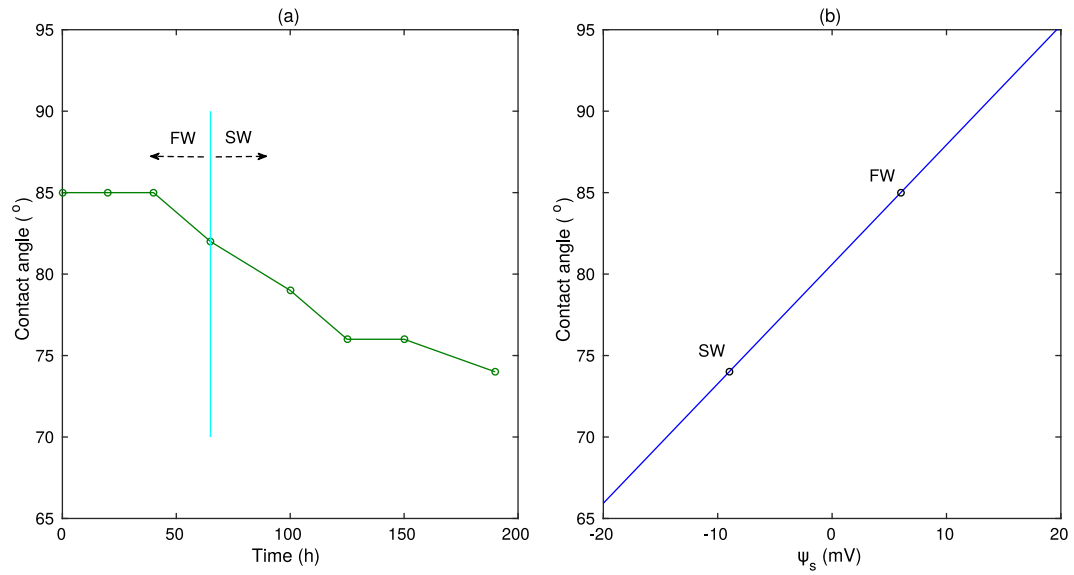


Fig. 15. (a) Experimental data showing contact angle variations on a limestone patch exposed to Formation Water (FW) and Sea Water (SW) (Mahani et al., 2015b) and (b) model that expresses the changes in contact angle as a function of surface potential.

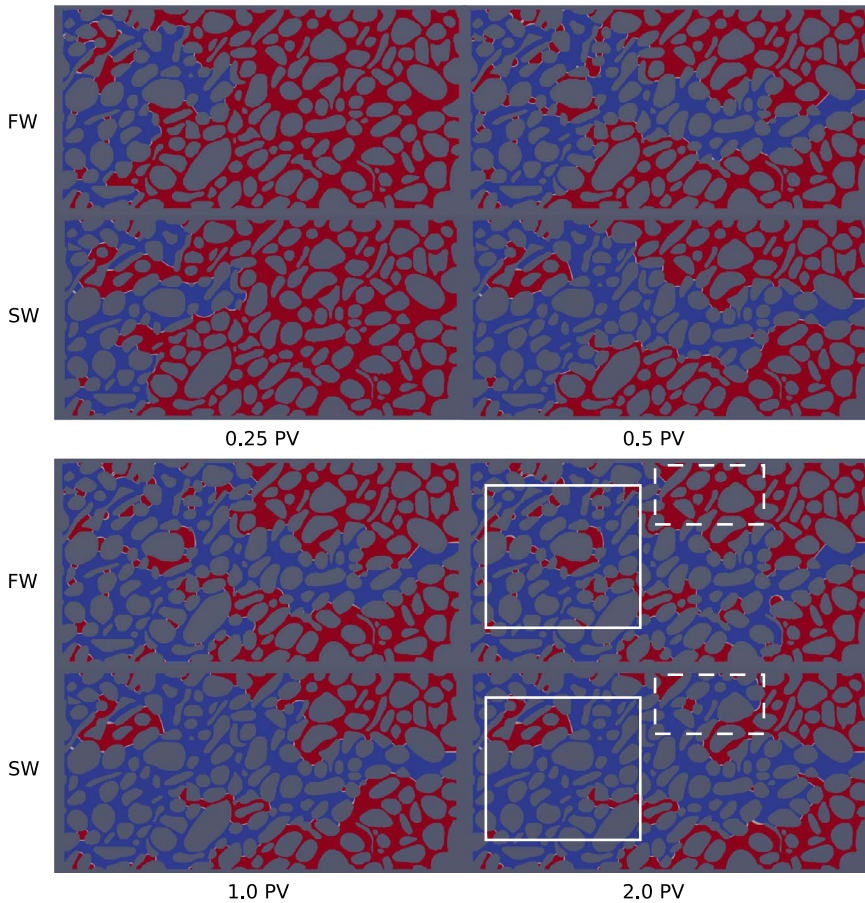


Fig. 16. Evolution of indicator function  $\alpha$  during Formation Water (FW) flooding and Sea Water (SW) flooding in a complex 2D porous media (Fig. 14) at different times corresponding to 0.25, 0.5, 1 and 2 Pore Volume (PV) injected. We observe two effects of wettability change: (1) a smaller number of oil clusters left after invasion (solid rectangle) and (2) a larger number of pore invaded (dashed rectangle).

increase of oil recovery of 15.2% for SW and 20.9% for FW–SW.

Our investigation shows that wettability change induced by surface complexation during low-salinity flooding can result in an improvement of pore-scale sweep efficiency. This has been previously observed in experimental studies on sandstone core-plug (Kumar and Mohanty, 2011; Zhang and Morrow, 2006; Zhang et al., 2007), but was associated with selective plugging via clay swelling (Bernard, 2011; Zhang and Morrow, 2006). Our study suggests that this improvement of sweep

efficiency could also be applied to carbonate reservoir, and be induced by the temporal evolution of the contact angle. This changes during LSF the set of pores and throats that become accessible to the invaded phase.

#### 4. Concluding remarks

A novel pore-scale reactive transport model has been developed and



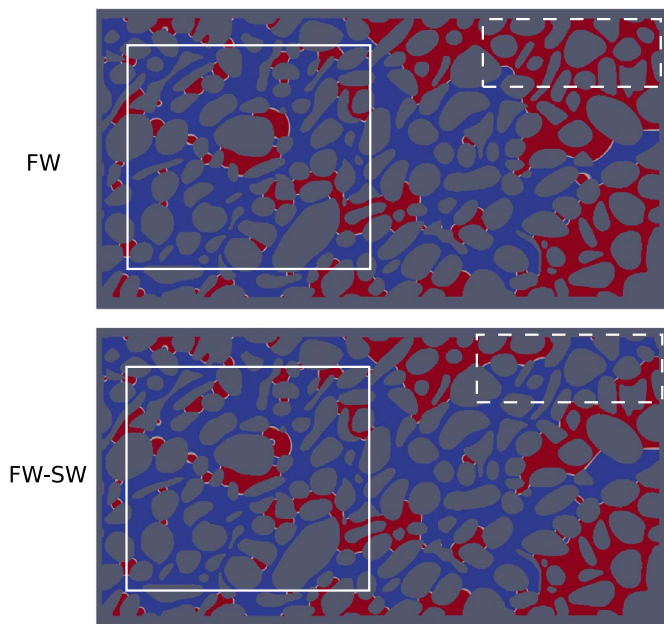


**Fig. 17.** Comparison between phase distribution for Formation Water (FW) flooding only and for Formation Water flooding followed by Sea Water (FW-SW) flooding in a complex 2D porous media (Fig. 14) after 4 injected pore volume. We observe that the amount and form of oil clusters left in the pore space after invasion (solid rectangle) remain mostly unchanged but that a greater number of pores have been invaded (dashed rectangle).

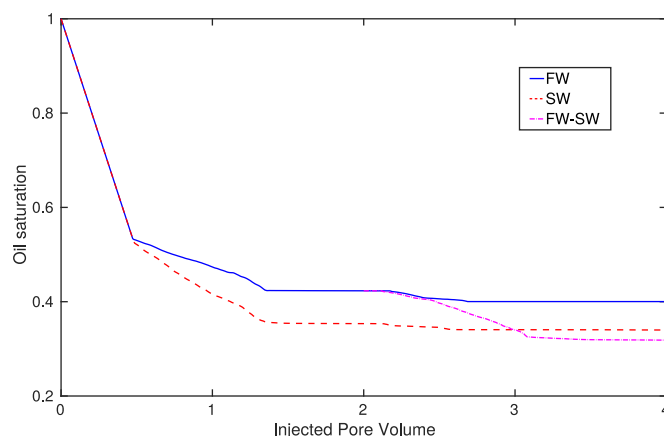


**Fig. 18.** Evolution of oil saturation during Formation Water (FW) flooding, Sea Water (SW) flooding and Formation Water flooding followed by Sea Water flooding (FW-SW) in a complex 2D pore structure (Fig. 14). The final oil saturations are  $S_{or}(FW) = 0.402$ ,  $S_{or}(SW) = 0.341$  and  $S_{or}(FW-SW) = 0.318$ , respectively.

validate, with the aim of providing new insights into wettability alteration by surface complexation as a mechanism of LSF, using 3D and 2D simulations. Based on the five applications considered here, we propose the following key conclusions:

- The change of surface potential at the calcite/water interface is not driven by the pH of the injected water, but by the concentration of PDI such as  $Ca^{+2}$  and  $Mg^{+2}$ . For the water compositions considered here, the concentration of  $SO_4^{-2}$  has only a small impact.
- Our numerical model is able to reproduce the evolution of the oil droplet shape with time during detachment from a clay patch. For this, the molecular diffusion near the surface of the solid need to be fitted to take into account electrostatic effect.
- On simple 2D models, e.g. a square pore and a  $3 \times 3$  micro-models, we show that our numerical model is convergent.
- A sensitivity analysis carried out for the  $3 \times 3$  micro-model show that the most important parameters controlling the residual oil

saturation are the velocity at which water is injected and the near-surface diffusion. We further show that the LSE is only observed if the transport regime is such that diffusion has a smaller or similar time-scale as advection, so that the low-salinity water has time to diffuse into the thin water film separating the oil and mineral surfaces and can induce a change in contact angle.

- By performing simulation on a complex 2D porous medium, we show that our numerical model is able to explain an increase of pore-scale sweep efficiency with LSF.

More generally, the results of our simulations highlight two effects of wettability alteration due to surface complexation during LSF, namely a decrease in the amount of residual oil left in the pore space after invasion and an increase of the number of pores that are invaded. The former is simply a consequence of calcite being more water-wet, but the latter is induced by the temporal evolution of contact angle and cannot be captured readily in static or quasi-dynamic pore-network models. This dynamic effect changes the set of pores and throats that become accessible to the invading brine during LSF. However, our model was not able to simulate the remobilisation mechanism observed when injecting low-salinity water after formation water (Bartels et al., 2017). Including thin film hydrodynamics (Abu-Al-Saud et al., 2017) and electrostatic effect inside the thin film (Joekear-Niasar and Mahani, 2017) could potentially solve this issue.

Our numerical modelling gives new insights into several mechanisms inducing an increase in oil recovery during low-salinity flooding. We have focused on the impact of several parameters, namely the water composition, the injected velocity, the contact angle model and the diffusivity in the thin film. Since our model can be parameterized easily, it can be used to study the impact of other factors such as oil and mineral compositions. For example, the evolution functions of contact angle with surface potential that we used in our examples were only calibrated with two data points. If more data points are made available, the evolution function can be obtained by interpolation and the contact angle model can be replaced with a more sophisticated approximation. Future work could focus on comparison with experimental observation on micro-models (Bartels et al., 2017). Then, our numerical model could be fully deployed to perform detailed sensitivity analysis on 3D micro-CT images, for example to develop quantitative and semi-quantitative rules that guide invasion by low-salinity water for pore network modelling studies (Watson et al., 2017).

## Acknowledgement

We would like to thank Petrobras and Shell for their sponsorship of the ICCR program and the permission to publish this work from the ReactCarb project. Sebastian Geiger further thanks the Energi Simulation Foundation for supporting his chair programme.

## References

- Abu-Al-Saud, M.O., Riaz, A., Tchalepi, H.A., 2017. Multiscale level-set method for accurate modeling of immiscible two-phase flow with deposited thin films on solid surfaces. *J. Comput. Phys.* 333, 297–320.
- Al-Mahrouqi, D., Vinogradov, J., Jackson, M.D., 2017. Zeta potential of artificial and natural calcite in aqueous solution. *Adv. Colloid Interface Sci.* 240, 60–76.
- Alhashmi, Z., Blunt, M.J., Bijeljic, B., 2015. Reactive transport in porous media: a comparison of model prediction with laboratory visualization. *J. Contam. Hydrol.* 179, 171–181.
- Alrouhnan, A., Vinogradov, J., Jackson, M.D., 2016. Zeta potential of intact natural limestone: impact of potential-determining ions Ca, Mg and  $SO_4$ . *Colloids Surf., A* 493, 83–98.
- Austad, T., Rezaeioudoust, A., Puntervold, T., 2010. Chemical mechanism of low-salinity waterflooding in sandstone reservoirs. *Proceedings of the 2010 SPE Improved Oil Recovery Symposium*, 24–28 April, Tulsa, Oklahoma, USA. <http://dx.doi.org/10.2118/129767-MS>.
- Bartels, W., Mahani, H., Berg, S., Menezes, R., van der Hoeve, J., Fadili, A., 2017. Oil configuration in high-salinity and low-salinity conditions at pore scale: a parametric investigation by use of a single-channel micromodel. *SPE Journal*. <http://dx.doi.org/10.2118/181386-PA>.
- Berg, S., Cense, A.W., Jansen, E., Bakker, K., 2010. Direct experimental evidence of

- wettability modification by low salinity. *Petrophysics* 51 (5), 314–322.
- Bernard, G.G., 2011. Effect of floodwater salinity on recovery of oil from cores containing clays. *Proceedings of the 2011 SPE California Regional Meeting*, 26–27 October, Los Angeles, California, USA. <http://dx.doi.org/10.2118/1725-MS>.
- Bijeljic, B., Raeini, A., Mostaghimi, P., 2013. Predictions of non-Fickian solute transport in different class of porous media using direct simulation on pore-scale images. *Phys. Rev. E* 87 (1).
- Blunt, M.J., King, P., 1991. Relative permeabilities from two- and three-dimensional pore network modelling. *Transp. Porous Med.* 6, 407–433.
- Brackbill, J.U., Kothe, D.B., Zemach, C., 1992. A continuum method for modeling surface tension. *J. Comput. Phys.* 100 (2), 335–354.
- Bradbury, M.H., Baeyens, B., 1997. A mechanistic description of ni and zn sorption on namontmorillonite. part ii: modelling. *J. Contam. Hydrol.* 27, 223–248.
- Brady, P.V., Krumhansl, J.L., 2012. A surface complexation model of oil-brine-sandstone interface at 100 °C: low salinity waterflooding. *J. Pet. Sci. Eng.* 81, 171–176.
- Brady, P.V., Krumhansl, J.L., Mariner, P.E., 2012. Surface complexation modeling for improved oil recovery. *Proceedings of the 2012 SPE Improved Oil Recovery Symposium*, 14–18 April, Tulsa, Oklahoma, USA. <http://dx.doi.org/10.2188/153744-MS>.
- Buckley, J.S., Takamura, K., Morrow, N.R., 1989. Influence of electrical surface charges on the wetting properties of crude oils. *SPE Res. Eng.* 4 (3), 332–340.
- Carraiyrou, J., Mose, R., Behra, P., 2004. Operator-splitting procedures for reactive transport and comparison of mass balance errors. *J. Contam. Hydrol.* 68, 239–268.
- Chen, Q., Mercer, D., Webb, K., 2010. NMR study on pore occupancy and wettability modification during low salinity waterflooding. *Proceeding of the 24th International Symposium of Core Analysis*, 4–7 October 2010, Halifax, Canada. Paper SCA 2010-27.
- Danckwerts, P.V., 1970. *Gas-liquid Reaction*. McGraw-Hill, New-York, New-York.
- Deising, D., Marschall, H., Bothe, D., 2016. A unified single-field model framework for Volume-Of-Fluid simulations of interfacial species transfer applied to bubbly flow. *Chem. Eng. Sci.* 139, 173–195.
- Francois, M.M., Cummins, S.J., Dendy, E.D., Kothe, D.B., Sicilan, J.M., Williams, M.W., 2006. A balanced-force algorithm for continuous and sharp interfacial surface tension models within a volume tracking framework. *J. Comput. Phys.* 213 (1), 141–173.
- Gerlach, D., Tomar, G., Biswas, G., Durst, F., 2006. Comparison of volume-of-fluid method for surface tension-dominant two-phase flows. *Int. J. Heat Mass Transfer* 49, 740–754.
- Goldberg, S., 2013. Surface complex modelling. *Ref. Module in Earth Syst. Environ. Sci.* 1–14. <http://dx.doi.org/10.1016/B978-0-12-409548-9.05311-2>.
- Gramling, C.M., Harvey, C.M., Meigs, L.C., 2002. Reactive transport in porous media: a comparison of model prediction with laboratory visualization. *Environ. Sci. Technol.* 36 (11), 2508–2514.
- Gravelleau, M., 2016. Pore scale simulation of mass transfer across immiscible interfaces. Master's thesis. Energy Resources Engineering, Stanford University.
- Han, L.H., Gu, Y.G., 2014. Optimization of miscible CO<sub>2</sub> water-alternating-gas injection in the Bakken formation. *Energy Fuels* 28 (11), 6811–6819.
- Haroun, Y., Legendre, D., Raynal, L., 2010. Volume of fluid method for interfacial reactive mass transfer: application to stable liquid film. *Chem. Eng. Sci.* 65, 2896–2909.
- Heberling, F., Trainor, T.P., Lützenkirchen, J., Eng, P., Denecke, M.A., Bosbach, D., 2011. Structure and reactivity of the water-calcite interface. *J. Colloid Interface Sci.* 354 (2), 843–857.
- Hirt, C.W., Nichols, B.D., 1981. Volume-Of-Fluid (VOF) method for the dynamic of free boundaries. *J. Comput. Phys.* 39 (1), 201–225.
- Hosa, A., Curtis, A., Wood, R., 2016. Calibrating lattice boltzmann flow simulations and estimating uncertainty in the permeability of complex porous media. *Adv. Water Resour.* 94, 60–74.
- Hunter, R.J., 1981. *Zeta Potential in Colloid Science: Principles and Applications*. Academic Press, New-York.
- Israelachvili, J., 1985. *Intermolecular and Surface Forces*. Academic Press, New-York.
- Issa, R., Ahmadi-Befrui, B., Beshay, K., Gosman, A., 1985. Solution of the implicitly discretised reacting flow equations by operator-splitting. *J. Comput. Phys.* 93 (2), 388–410.
- Jackson, M.D., Al-Mahrouqi, D., Vinogradov, J., 2016. Zeta potential in oil-water-carbonate systems and its impact on oil recovery during controlled salinity waterflooding. *Sci. Rep.* 6, 37363.
- Jackson, M.D., Vinogradov, J., Hamon, G., Chamerois, M., 2016. Evidence, mechanism and improved understanding of controlled salinity waterflooding part i: sandstones. *Fuel* 185, 772–793.
- Joekar-Niasar, V., Hassanizadeh, S.M., Dahle, H.K., 2010. Non-equilibrium effect in capillarity and interfacial area in two-phase flow: dynamic pore network modelling. *J. Fluid Mech.* 655, 38–71.
- Joekar-Niasar, V., Mahani, H., 2017. Nonmonotonic pressure field induced by ionic diffusion in charged thin films. *Ind. Eng. Chem. Res.* <http://dx.doi.org/10.1021/acs.iecr.6b00842>.
- Kallel, W., van Dijke, M.I.J., Sorbie, K.S., Wood, R., 2017. Pore-scale modeling of wettability alteration during primary drainage. *Water Resour. Res.* <http://dx.doi.org/10.1002/2016WR018703>.
- Kallel, W., van Dijke, M.I.J., Sorbie, K.S., Wood, R., Jiang, Z., Harland, S., 2016. Modelling the effect of wettability distribution on oil recovery from microporous carbonate. *Adv. Water Resour.* 95, 317–328.
- Karadimitriou, N.K., Joekar-Niasar, V., Brizuela, O.G., 2017. Hydro-dynamic solute transport under two-phase flow conditions. *Sci. Rep.* 7, 6624.
- Kumar, R., Mohanty, K.K., 2011. Sweep efficiency of heavy oil recovery by chemical methods. *Proceedings of the 2011 SPE Annual Technical Conference and Exhibition*, 30 October–2 November, Denver, Colorado, USA. <http://dx.doi.org/10.2118/146839>.
- van Leer, B., 1974. Towards the ultimate conservative difference scheme. II. Monotonicity and conservation combined in a second-order scheme. *J. Comput. Phys.* 14 (4), 361–370.
- Lenormand, R., Touboul, E., Zarcone, C., 1988. Numerical models and experiments on immiscible displacements in porous media. *J. Fluid Mech.* 189, 165–187.
- Li, Y., Gregory, S., 1973. Diffusion of ions in seawater and in deep sea-sediments. *Geochim. Cosmochim. Acta* 38, 703–714.
- Mahani, H., Berg, S., Ilic, D., Bartels, W.-B., Joekar-Niasar, V., 2015. Kinetics of low-salinity-flooding effect. *SPE J.* 20 (1), 8–20.
- Mahani, H., Levy Keya, A., Berg, S., Bartels, W., Nasralla, R., Rossen, W.R., 2015. Insights into the mechanism of wettability alteration by Low-Salinity Flooding (LSF) in carbonates. *Energy Fuels* 29, 1352–1367.
- Mahani, H., Levy keya, A., Berg, S., Nasralla, R., 2016. Electrokinetics of carbonate/brine interface in low-salinity waterflooding: effect of brine salinity, composition, rock type, and pH on  $\zeta$ -potential and a surface-complexation model. *SPE J.* <http://dx.doi.org/10.2118/181745-PA>.
- Mahani, H., Menezes, R., Berg, S., Fadili, A., Nasralla, R., Voskov, D., Joekar-Niasar, V., 2017. Insights into the impact of temperature on the wettability alteration by low salinity in carbonate rocks. *Energy Fuel.* <http://dx.doi.org/10.1021/acs.energyfuels>.
- Marschall, H., Hinterberger, K., Schüler, C., Habla, F., Hinrichsen, O., 2012. Numerical simulation of species transfer across fluid interfaces in free-surface flows using OpenFOAM. *Chem. Eng. Sci.* 78, 111–127.
- McGuire, P.L., Chatham, J.R., Paskvan, F.K., Sommer, D.M., Carini, F.H., 2005. Low salinity oil recovery: an exciting new EOR opportunity for Alaska's North Slope. *Proceeding of the 2005 SPE Western Regional Meeting*, 30 March–1 April, Irvine, California, USA. <http://dx.doi.org/10.2118/93903-MS>.
- Meakin, P., Tartakovsky, A.M., 2009. Modeling and simulation of pore-scale multiphase flow and reactive transport in fractured and porous media. *Rev. Geophys.* 47 (RG3002).
- Myers, R.H., Montgomery, D.C., Anderson-Cook, C.M., 2009. *Response Surface Methodology: Process and Product Optimization Using Design of Experiments*, 3rd. John Wiley and Sons, Inc., Oxford, U. K.
- Nordhaug, H.F., Celia, M., Dahle, H.K., 2003. A pore network model for calculation of interfacial velocities. *Adv. Water Resour.* 26 (10), 1061–1074.
- Ogata, A., Banks, R.B., 1961. A solution of the differential equation of longitudinal dispersion in porous media. *Professional Paper 411-A*. U.S. Geological Survey.
- Pan, C., Hilpert, M., Miller, C.T., 2004. Lattice-Boltzmann simulation of two-phase flow in porous media. *Water Resour. Res.* 40 (1).
- Patankar, S.V., Spalding, D.B., 1972. A calculation procedure for heat, mass and momentum transfer in three-dimensional parabolic flows. *Int. J. Heat Mass Transfer* 15 (10), 1787–1806.
- Pavuluri, S., Maes, J., Geiger, S., Doster, F., 2017. Benchmark numerical investigation of spontaneous imbibition in a capillary using different volume-of-fluid formulations. *Comput. Fluids*.
- Pokrovsky, O.S., Mielczarski, J.A., Barres, O., Schott, J., 2000. Surface speciation models of calcite and dolomite/aqueous solution interfaces and their spectroscopic evaluation. *Langmuir* 16 (6), 2677–26887.
- Popinet, S., 2009. An accurate adaptive solver for surface-tension-driven interfacial flows. *J. Comput. Phys.* 228, 5838–5866.
- Raeini, A., Blunt, M.J., Bijeljic, B., 2012. Modelling two-phase flow in porous media at the pore-scale using the volume-of-fluid method. *J. Comput. Phys.* 231 (17), 5653–5668.
- Scardovelli, R., Zaleski, S., 1999. Direct numerical simulation of free-surface and interfacial flow. *Annu. Rev. Fluid Mech.* 31, 567–603.
- Soulaire, C., Tchepel, H.A., 2016. Micro-continuum approach for pore-scale simulation of subsurface processes. *Transp. Porous Med.* 113 (3), 431–456.
- Steeffel, C.I., DePaolo, D.J., Lichtner, P.C., 2005. Reactive transport modeling: an essential tool and a new research approach for the earth sciences. *Earth Planet. Sci. Lett.* 240 (3–4), 539–558.
- Steeffel, C.I., Molins, S., Trebotich, D., 2013. Pore scale processes associated with subsurface CO<sub>2</sub> injection and sequestration. *Rev. Mineral. Geochem.* 77 (1), 259–303.
- Tang, G., Morrow, N.R., 1997. Salinity, temperature, oil composition, and oil composition by waterflooding. *SPE Res. Eng.* 12 (4), 269–276.
- Tang, G., Morrow, N.R., 1999. Influence of brine composition and fines migration on crude oil/brine/rock interactions and oil recovery. *J. Petrol. Sci. Eng.* 24 (2–4), 99–111.
- Tang, G., Morrow, N.R., 2002. Injection of dilute brine and crude oil/brine/rock interactions. *Environ. Mech.* 129, 171–179.
- Tartakovsky, A.M., Meakin, P., 2006. Pore scale modeling of immiscible and miscible fluid flows using smoothed particle hydrodynamics. *Adv. Water Resour.* 29 (10), 1464–1478.
- Ubbink, O., Issa, R.I., 1999. A method for capturing sharp fluid interfaces on arbitrary meshes. *J. Comput. Phys.* 153, 26–50.
- Watson, M., Bondino, I., Hammon, G., McDougall, S.R., 2017. A pore-scale investigation of low-salinity waterflooding in porous media: uniformly wetted systems. *Transp. Porous Med.* <http://dx.doi.org/10.1007/s11242-017-0854-8>.
- Zaretskiy, Y., Geiger, S., Sorbie, K., 2012. Direct numerical simulation of pore-scale reactive transport: applications to wettability alteration during two-phase flow. *Int. J. Oil Gas Coal T.* 5 (2–3), 142–156.
- Zaretskiy, Y., Geiger, S., Sorbie, K., Förster, M., 2010. Efficient flow and transport simulations in reconstructed 3D pore geometries. *Adv. Water Resour.* 33, 1508–1516.
- Zhang, Y., Morrow, N.R., 2006. Comparison of secondary and tertiary recovery with change in injection brine composition for crude-oil/sandstone combinations. *Proceedings of the 2006 SPE/DOE Symposium on Improved Oil Recovery*, 22–26 April, Tulsa, Oklahoma, USA. <http://dx.doi.org/10.2118/99757-MS>.
- Zhang, Y., Xie, X., Morrow, N.R., 2007. Waterflood performance by injection of brine with different salinity for reservoir cores. *Proceedings of the 2007 SPE Annual Technical Conference and Exhibition*, 11–14 November, Anaheim, California, USA.